Available online at www.sciencedirect.com

ScienceDirect

Geochimica et Cosmochimica Acta 329 (2022) 231–255

Geochimica et Cosmochimica Acta

www.elsevier.com/locate/gca

Experimental determination of hydrogen isotope exchange rates between methane and water under hydrothermal conditions

Andrew C. Turner [a,b,*], Nicholas J. Pester [a,b], Markus Bill [b], Mark E. Conrad [b], Kevin G. Knauss [b], Daniel A. Stolper [a,b]

[a] Department of Earth and Planetary Science, University of California, Berkeley, CA 94720, USA
[b] Energy Geosciences Division, Lawrence Berkeley National Laboratory, 1 Cyclotron Road, Berkeley, CA 94720, USA

Received 16 November 2021; accepted in revised form 26 April 2022; Available online 2 May 2022

Abstract

The hydrogen isotopic composition of methane (CH_4) is used as a fingerprint of gas origins. Exchange of hydrogen isotopes between CH_4 and liquid water has been proposed to occur in both low- and high-temperature settings. However, despite environmental evidence for hydrogen isotope exchange between CH_4 and liquid water, there are few experimental constraints on the kinetics of this process. We present results from hydrothermal experiments conducted to constrain the kinetics of hydrogen isotope exchange between CH_4 and supercritical water. Seven isothermal experiments were performed over a temperature range of 376–420 °C in which deuterium-enriched water and CH_4 were reacted in flexible gold reaction cell systems. Rates of exchange were determined by measuring the change in the δD of CH_4 over the time course of an experiment. Regression of derived second order rate constants (k_r) vs. 1000/T (i.e., an Arrhenius plot) yields the following equation: $\ln(k_r) = -17.32$ (±4.08, 1 s.e.) × 1000/T + 3.19 (±6.01, 1 s.e.) (units of k_r of sec^{-1} $[mol/L]^{-1}$), equivalent to an activation energy of 144.0 ± 33.9 kJ/mol (1 s.e.). These results indicate that without catalysts, CH_4 will not exchange hydrogen isotopes with liquid water on a timescale shorter than the age of the Earth (i.e., billions of years) at temperatures below 100–125 °C. Exchange at or below these temperatures is thought to occur due to the activity of life, and thus hydrogen isotopic equilibrium between methane and water may be a biosignature at low temperatures on Earth (in the present or the past) and on other planetary bodies. At temperatures ranging from 125 to 200 °C, hydrogen isotope exchange between CH_4 and liquid water can occur on timescales of millions to hundreds of thousands of years, indicating that in thermogenic natural gas systems CH_4 may isotopically equilibrate with water and achieve equilibrium isotopic compositions. Finally, the kinetics indicate that in deep-sea hydrothermal systems, the hydrogen (and thus clumped) isotopic composition of CH_4 is likely set by formation and/or storage conditions isolated from the active flow regime. The determined kinetics indicate that once methane is entrained in circulating fluids, the expected time-temperature pathways are insufficient for measurable hydrogen isotope exchange between CH_4 and water to occur.

Keywords: Hydrogen isotope exchange; Methane; Hydrothermal systems; Isotope kinetics

1. INTRODUCTION

The hydrogen isotopic composition of methane is commonly used as a fingerprint of a gas's origins (e.g., thermogenic vs. microbial). This approach relies on the assumption that, following formation, the isotopic composition of the

* Corresponding author at: Department of Earth and Planetary Science, University of California, Berkeley, CA 94720, USA.
E-mail address: acturner@berkeley.edu (A.C. Turner).

https://doi.org/10.1016/j.gca.2022.04.029
0016-7037/

methane does not change during migration and/or storage in Earth's crust. The hydrogen isotopic composition of methane could be modified if it is able to exchange hydrogen isotopes with other hydrogen-bearing species. Here we focus on the potential role that hydrogen isotope exchange reactions between methane and liquid water may play in (re)setting the isotopic composition of methane in nature.

Exchange of hydrogen isotopes between methane and liquid water has been proposed to occur in both low- and high-temperature settings. For example, microbial organisms have been proposed to catalyze methane-water hydrogen isotope exchange reactions (e.g., Stolper et al., 2015; Wang et al., 2015; Douglas et al., 2016; Okumura et al., 2016; Gropp et al., 2021; Jautzy et al., 2021; Ono et al., 2021; Turner et al., 2021; Wegener et al., 2021). The maximum known growth temperature for microorganisms is 122 °C (specifically a methanogen; Takai et al., 2008), placing this as the current upper limit for biologically mediated CH_4-H_2O hydrogen isotope exchange. At higher temperatures (>150 °C), abiotic hydrogen isotope exchange reactions between methane and water in sedimentary (Burruss and Laughrey, 2010; Xie et al., 2021) and hydrothermal systems (Horibe and Craig, 1995; Reeves et al., 2012; Wang et al., 2018; Beaudry et al., 2021) have also been proposed to occur.

Despite environmental evidence for abiotic hydrogen isotope exchange between methane and water, there are few experimental constraints on the kinetics of this process. Such constraints are needed to predict and/or reconstruct the thermal histories required for exchange to occur. We are aware of two experimental constraints: The first is a single data point published in an abstract by Koepp (1978) after methane was heated at 200 °C (for 400 days) in the presence of D_2O in a stainless steel reactor. Although the methane in this experiment is often assumed (when used in other studies) to have reacted with liquid water, based on the experimental details provided in the technical report on which the abstract is based (Köpp, 1977), the experiment took place in a system in which >99.9% of the methane existed in the gas phase and 1% of the volume of the reactor was occupied by liquid water. As will be discussed in more detail below, we believe this experiment provides limited constraints on the exchange rates between methane and liquid water.

The second constraint is from Reeves et al. (2012) in which methane, ethane, propane, *n*-butane, and *n*-pentane were dissolved in isotopically labeled water and held at 323 °C and 35 MPa in a flexible gold reaction cell. Reeves et al. (2012) observed shifts in the δD of methane of up to 32‰ over the course of the experiments (up to 112 days). They suggested these shifts were potentially due to hydrogen isotope exchange with liquid water as opposed to in situ generation of methane. However, they did not calculate a rate for this exchange. Wang et al. (2018) used the data of Reeves et al. (2012), assumed the methane δD shift was due to hydrogen isotope exchange with water, and estimated a 'best guess' for the timescale of the reaction to reach 50% equilibration was ~24 years. Wang et al. (2018) noted the uncertainty in the calculated rate was potentially several orders of magnitude. Wang et al. (2018) then used this rate (at 323 °C), along with the data point from Koepp (1978) (at 200 °C), to estimate isotope exchange rates between methane and liquid water as a function of temperature (their Fig. 4)—the equation for this line was subsequently given in Beaudry et al. (2021).

Here we present new experimental results on hydrogen isotope exchange rates between dissolved methane and supercritical water. We specifically provide new experimental constraints over a temperature range of 376–420 °C in single-phase hydrothermal systems in which pure methane was dissolved in isotopically labeled supercritical water and hydrogen isotope exchange rates measured. Then, using these exchange rates, we evaluate the likely environmental conditions under which methane and water will or will not exchange hydrogen isotopes over various timescales in low-temperature systems supporting microbial life and in higher-temperature thermogenic gas systems and marine hydrothermal systems.

2. METHODS

2.1. Experimental setup

Experiments were conducted at constant pressure and temperature in flexible gold reaction cells sealed with a passivated (oxidized) titanium head (Seyfried et al., 1979). Prior to use, the gold and titanium parts were cleaned as follows: gold cells were filled with a boiling 1.5 N HCl solution and allowed to stand for 30 min. The cell was then washed with deionized water (high-purity 18.2 MΩ-cm) and the gold annealed at 600 °C for 15 min. Boiling 8 N nitric acid was added to titanium parts and left for 30 min. These parts were then rinsed in deionized water as above and then held overnight at 400 °C to form a passivated oxide layer. In some experiments we did not completely disassemble (unseal) the gold cell used in a previous experiment in order to (acid) clean the gold/titanium surfaces. Rather, the exit tube was removed, remaining water was evaporated from the cell at 200 °C, and fresh δD-enriched starting water was introduced (see below). We note that upon conclusion of the first experiments, no residue or precipitant was observed within the gold cells.

Experimental conditions were always a single phase with methane dissolved in supercritical water. These reactors allow the experimental fluid to be sampled multiple times over the course of an experiment at constant pressure and temperature. Experimental details including apparatus design, experimental setup, and sampling procedures are given in Pester et al. (2018). We note that a similar system was used in the experiments of Reeves et al. (2012). We briefly review the methods here but refer the reader to Pester et al. (2018) for a detailed overview of the experimental approach.

Briefly, a gold cell was first filled with δD-enriched water (~1000–5000‰ depending on the experiment), which was made by mixing 99.9% D_2O (Sigma-Aldrich) with high-purity 18.2 MΩ-cm deionized water. We then sealed the cell with a titanium closure. Before and during the sealing of the gold cell, the liquid was sparged with argon (99.999%) to remove other atmospheric gases from the system. The

sealed cell was then loaded into a steel pressure vessel, confining water added external to the cell, and the vessel sealed and placed into a furnace. Following removal of residual headspace gas from the gold cell, the system was pressure tested to ensure the steel vessel was not leaking. Once the testing pressure was relieved, water was removed from the gold cell, and a charge of methane (99.97%) was added to the cell from a gas cylinder. Finally, the system was heated to the desired pressure and temperature (Table 1). Pressures at a given temperature were selected such that the density of water was the same in all experiments, 0.58 g/ml. In one experiment, experiment 4, we first heated the experiment to 416 °C for 47 days before cooling it to 394 °C for 70 days. For this experiment, each temperature is treated as a separate experiment (termed experiment 4 part 1 and experiment 4 part 2 respectively).

An experiment was sampled as follows. First, ~1 ml of experimental fluid was taken and discarded in order to purge the sampling tube. Following this, samples were taken for chemical and isotopic analyses. For isotopic measurements, fluid was taken into a bottle sealed with a butyl rubber stopper and then stored until analyzed. Methane exsolves from the fluid following addition to the sealed vial. Prior to sample addition, we purged bottles with 99.999% He. For analysis of dissolved gas concentrations, an additional sample was taken into a gas-tight syringe and the headspace gas immediately injected into a gas chromatograph (see below). During sampling of most experiments, pressure in the confining volume was maintained using a Teledyne (ISCO) high-pressure syringe pump. In the first few experiments, only an air-driven (Sprague) pump was available. In these cases, to avoid pressure surges during sampling, the system was connected to a pre-pressurized (water-filled) external volume to buffer pressure drop during sampling. For the latter, pressure decreases were <10 bar during sampling, and pressure was then increased following sampling back to the desired experimental pressure.

We monitored all experiments for the development of leaks between the gold cell and confining fluid. This is often done using dilute NaCl solutions in the experimental fluid (vs. none in the confining fluid). We did not add NaCl at any concentration in order to avoid any potential effects on reaction rates due to the presence of these solutes. We instead checked for leaks as follows: In all experiments we measured the δD of the fluid within the gold cell over the course of the experiment and used this to evaluate a leak. Additionally, in some experiments, krypton (Kr) was added to the confining fluid outside of the gold cell and the Kr concentration of the gold cell fluid was measured by gas chromatography. Communication between the confining water and fluid in the gold cell is recognized if the δD_{H2O} of the gold cell fluid changes (as the confining water is not enriched in δD) and/or the dissolved Kr concentration increases with time in the sampled fluids.

2.2. Mass spectrometric methods

The δD of CH_4 (δD_{CH4}) was analyzed at the Center for Isotope Geochemistry at the Lawrence Berkeley National Laboratory using a Thermo Scientific Trace GC Ultra system connected to a Delta V Plus isotope-ratio mass spectrometer (GC-IRMS: Thermo Fisher Scientific) as described in Turner et al. (2021). Details of sample measurement and standardization are given in Appendix A1.

2.3. Laser spectroscopic methods

The δD of liquid water samples from our experiments (δD_{H2O}) was measured at the Center for Isotope Geochemistry at the Lawrence Berkeley National Laboratory using a Los Gatos Research (LGR) Isotopic Water Analyzer IWA-35-EP (Model # 912-0026-0001). Samples had δD_{H2O} values of ~1000 to 5000‰, which are outside the range of our available water standards (maximum of +860.1‰). As such, samples were diluted 10× with laboratory Milli-Q waters (also measured for δD_{H2O}) and the value of the original water calculated based on the isotopic composition of the undiluted endmember, final mixture δD_{H2O} value, and the dilution ratio. Standardization was achieved using three internal water standards (from −161.3‰ to 642.4‰; supplied by LGR) such that diluted sample δD_{H2O} were intermediate to the standards used. Final correction of measured sample δD_{H2O} value was performed using software provided by LGR (LGR LWIA Post Analysis, version 3.1.0.9).

2.4. Concentration determinations

Concentrations of dissolved gases (CH_4, H_2, CO_2, Kr) were measured via gas chromatography (Perkin Elmer Clarus 580). Fluid samples were collected in a gas-tight

Table 1
Summary of Experimental Results.

Experiment	T (°C)	P (bar)	Duration (days)	$\ln(k_r)$ (sec^{-1} $[mol/L]^{-1}$)	Uncertainty (1σ)[a]
Exp1	419.8	646	40.7	−21.61	0.106
Exp2	376.0	342	230.0	−23.09	0.010
Exp4.1[b]	416.4	652	47.1	−21.98	0.026
Exp4.2[b]	393.7	496	81.2	−23.38	0.039
Exp6[b]	412.4	625	125.6	−21.92	0.016
Exp7	404.8	563	163.2	−22.54	0.009
Exp8	419.0	637	197.0	−21.70	0.011

[a] Calculated as described in Section A5.
[b] Indicates a leak between the gold cell fluid and pressurizing fluid was observed; see Appendix A4.

syringe and the mass of water recorded. We diluted the exsolved headspace gas with carrier gas (either He or N_2 at 1 atm) to within the calibration range of a combined thermal conductivity detector (TCD) and flame ionization detector (FID) system and recorded the diluted gas volume. An aliquot of the gas was then injected onto the gas chromatograph. CH_4, H_2, and Kr concentrations were measured on the TCD after the gas passed through a GasPro PLOT column. CO_2 was separated using a Carboxen 1010 PLOT column and concentrations were measured with an FID/methanizer. Final dissolved gas concentrations were determined based on the mole fraction of gas measured in the headspace, the headspace volume, and the mass of the fluid sample.

2.5. Derivation of kinetic parameters

We assume that isotope exchange reactions proceed through the following reaction scheme and follow second-order reaction kinetics:

$$^{12}CH_4 + HDO \underset{k_r}{\overset{k_f}{\rightleftharpoons}} {}^{12}CH_3D + H_2O \quad (1)$$

In Eq. (1) k_f and k_r are rate constants for the forward and backward direction of the reaction as written (units of sec^{-1} $[mol/L]^{-1}$). In our experiments, the concentrations of HDO, H_2O, and $^{12}CH_4$ can be assumed to be constant. Thus, the rate of change of $^{12}CH_3D$ can be approximated following standard kinetic derivations (e.g., Criss et al., 1987; Gregory et al., 1989) and the change in δD_{CH4} vs. time (t) described as follows:

$$\frac{\delta D_{CH_4}(t) - \delta D_{CH_4;\,equilibrium}}{\delta D_{CH_4;\,initial} - \delta D_{CH_4;\,equilibrium}} = 1 - F = e^{-[H_2O]k_r t} \quad (2)$$

$[H_2O]$ is the concentration of water in mol/L. The 'equilibrium' subscript represents the isotopic composition of methane once it has reached hydrogen isotopic equilibrium with the fluid. F is the 'progress variable' and represents the fractional approach to isotopic equilibrium such that at the start of the reaction $F = 0$ and $1 - F = 1$. Once equilibrium is reached $F = 1$ and $1 - F = 0$ (Criss et al., 1987; Criss, 1999). For completeness, Eq. (2) is derived formally in Appendix A2 along with an equivalent result for $^{13}CH_3D$ exchange.

Use of Eq. (2) requires us to know $\delta D_{CH4;\,equilibrium}$ for a given experiment, which in turn requires knowledge of the hydrogen isotope equilibrium fractionation factor between methane and liquid (l) or supercritical (sc) water ($^{D}\alpha_{CH4(g)\text{-}H2O(l/sc)}$). We are unaware of a theoretical or experimental equation that describes this fractionation factor over the temperatures of interest to the work here (0–500 °C). As such, we calculated one based on constraints from prior theoretical and experimental work as described in Appendix A3 in detail. We now outline this in brief below.

Specifically, below the critical point, we use theoretical calculations of hydrogen isotope equilibrium between CH_4(g)-H_2(g) combined with those for H_2O(g)-H_2(g) based on Path Integral Monte Carlo calculations given in Turner et al. (2021) offset by constant values to fit experimental data. We then combine these with the calibration for $^{D}\alpha_{H2O(g)\text{-}H2O(l)}$ from Horita and Wesolowski (1994) to calculate $^{D}\alpha_{CH4(g)\text{-}H2O(l)}$—note that the calibration of Horita and Wesolowski (1994) is strictly only interpolatable based on experiments from 0.75 to 349 °C. However, they indicate this equation can be used from 0 to 374 °C as they fix $^{D}\alpha_{H2O\text{-}(g)\text{-}H2O(l)}$ to be equal to 1 at the critical point. We use the temperature dependence of theoretical equations as they allow for extrapolation beyond the experimental calibration for CH_4(g)-H_2(g) (3–200 °C) given in Turner et al. (2021) while preserving the expected temperature dependence.

Following Horita and Wesolowski (1994), we assume that at the critical point of water the hydrogen isotope fractionation factor between liquid water and water vapor approaches a value of 1 (i.e., become equal). Put another way, at the critical point, we assume that $^{D}\alpha_{CH4(g)\text{-}H2O(g)}$ and $^{D}\alpha_{CH4(g)\text{-}H2O(l)}$ are equal (as $^{D}\alpha_{H2O(g)\text{-}H2O(l)} = 1$). Above the critical point, and thus for supercritical fluids, we assume that the fractionation factor between methane and a supercritical fluid is equivalent to that between methane and water vapor—theoretical calculations indicate that at pressures to 1000 bar and 510 °C this introduces errors of less than 5‰ for the fractionation factor (Polyakov et al., 2006), which does not affect our presented results—these errors are due to the fact that the at high enough densities (e.g., above the critical density) supercritical fluids will exhibit properties distinct from the ideal gas, low pressure end-member. Regardless, we then use the theoretical fit of $^{D}\alpha_{CH4(g)\text{-}H2O(g)}$ to experimental describe the temperature dependence of $^{D}\alpha_{CH4(g)\text{-}H2O(sc)}$. More accurate approaches would require specifying both the temperature and pressure of the system to describe the supercritical fluid, but given the 5‰ variations this introduces, we consider our approach acceptable.

We then fit a polynomial to these curves to make a continuous function, which is given by:

$$1000 \times \ln {}^{D}\alpha_{CH_4(g)-H_2O(l/sc)} = \frac{1.4315 \times 10^{12}}{T^4} - \frac{1.7590 \times 10^{10}}{T^3} + \frac{6.4487 \times 10^{7}}{T^2} - \frac{1.2339 \times 10^{5}}{T} - 16.87 \quad (3)$$

In Eq. (3), the temperature (T) is in Kelvin. The 'l/sc' designates that this equation can be used for both liquids ('l') and supercritical ('sc') fluids. Our approach to determining Eq. (3) is displayed graphically in Fig. A2. We note that we do not use the equation for hydrogen isotopic equilibrium of methane and liquid water from Horibe and Craig (1995) because this calibration uses the calibration for hydrogen isotopic equilibrium between water vapor and liquid water from Horita and Wesolowski (1994), which, as discussed above, can only be used for waters from 0 °C to 374 °C (i.e., the critical point of water). Above 374 °C,

the fit of their calibration is an extrapolation and thus values that would be calculated for our experiments (which are above the critical point of pure water) may be inaccurate.

Returning to Eq. (2) and with the $\delta D_{CH4;\ equilibrium}$ now calculable, we then use the measured values of $\delta D_{CH4}(t)$ and $\delta D_{CH4;\ initial}$. Thus, the rate constant k_r multiplied by the concentration of water can be determined by linear regression of the experimental data using the following equation:

$$\ln\left(\frac{\delta D_{CH4}(t) - \delta D_{CH4;\ equilibrium}}{\delta D_{CH4;\ initial} - \delta D_{CH4;\ equilibrium}}\right) = \ln(1 - F) = -[H_2O]k_r t \quad (4)$$

In some experiments, we noted a leak developed between the external pressurizing fluid and the gold cell fluid (evidenced by changing δD_{H2O} values of the fluid in the gold cell). These experiments (specifically experiments 4.1, 4.2, and 6) are noted in Table 1 and Supplementary Table S1. For the fits we take the average δD of the experimental fluids (specifically the time weighted average δD of the water). We demonstrate in Appendix A4 that this approach does not affect the calculated rate constants in a way that impacts our interpretations (e.g., differences are less than ±2 standard error (s.e.) of the stated uncertainty on the rate constants).

3. RESULTS

3.1. Example experimental results

In Fig. 1 we provide an example of data from our longest duration experiment (230 days), which was held at 376 °C. Data for all experiments including temperature, pressure, sampling time, methane and water δD, and CO_2, H_2, and CH_4 concentrations are given in Table S1. The 376 °C experiment demonstrates a universal feature of our experiments: at the start of the reaction the δD of methane initially increases at a rate faster than in the later parts of the experiments. Following this initial period, δD_{CH4} increases at an effectively constant rate as, at low degree of reaction progress (maximum of 22% across all experiments), changes in δD_{CH4} vs. time are expected to follow an approximately linear relationship.

We assume that the initially faster increase in methane δD is due to the generation of small amounts of contaminant methane from the pyrolysis of trace organic contaminants that directly incorporate the high δD of the gold cell fluid (~5000‰). We tested for this explicitly by heating an experiment at 400 °C without methane added (i.e., a blank experiment) and examined the change in methane concentration with time. Methane increased in concentration and then stabilized to 0.2 mM after ~25–30 days into the

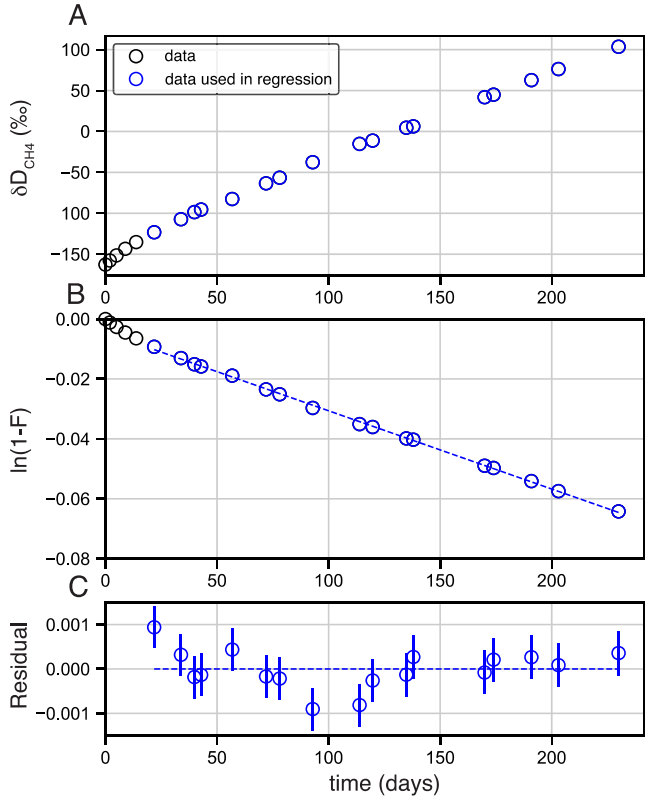

Fig. 1. An example of our experimental data from our longest experiment, experiment 2 (T = 376 °C). (A) δD_{CH4}, (B) ln(1 − F), and (C) the residual to the linear regression in (B). All are plotted vs. time (days). Error bars are ±1σ or smaller than the size of the point.

experiment (Fig. A1). For comparison, the experiments described above were conducted with concentrations between 20 and 120 mM methane (Table S1). Trace methane generation commonly occurs in hydrothermal experiments (e.g., McCollom, 2012) and so this observation was not unexpected. Additionally, in experiment 4, the first part of the experiment where the fluid was heated to 416 °C (experiment 4 pt. 1) shows this initial faster rate, but, after cooling later to 394 °C (experiment 4 pt. 2), a faster initial rate is not apparent. This is consistent with some initial methane generation occurring and going to completion at 416 °C before cooling the experiment to 394 °C. We note that we do not know the source of the generated methane, but it may represent a combination of contaminant organic carbon species present in the 99.97% methane used to charge the experiment, dissolved in the Milli-Q water or purchased D_2O solution, or alternatively a contaminant introduced during cleaning and assembly of the gold cell.

Based on this, we only fit data to the later part of experiments and exclude data from initial time periods with the faster increase in methane δD. The points chosen to be included in the fit were manually selected using the linear regression R^2 values, root mean square error, and visual assessment of the residuals of the fit of Eq. (4) to the data based on inclusion and exclusion of different points at the start of the experiment. Fits of $\ln(1 - F)$ vs. time for the experiments are given in Fig. 2. The data points for the experiments are provided in Table S1.

3.2. Temperature dependence of the rate constants

We calculated the values of k_r from regression of Eq. (4) to the data using a water concentration of 32.2 mol/L (equivalent to a density of 0.58 g/ml). Calculated rate constants and their associated uncertainties are given in Table 1. Uncertainties were calculated based on a Monte Carlo error propagation scheme (see Appendix A5).

We display the natural logarithm of the rate constants (units of $\ln(sec^{-1}\ [mol/L]^{-1})$ vs. $1000/T\ (K^{-1})$) in Fig. 3 in an Arrhenius plot. We observe, as expected, that rate constants decrease with decreasing temperature. A linear fit of these data (Fig. 3) yields an equation with slope of −17.32 (±4.08, 1 s.e.), intercept of 3.19 (±6.01, 1 s.e.), and covariance of −24.54:

$$\ln(k_r) = -17.32\left(\frac{1000}{T}\right) + 3.19 \quad (5)$$

This slope equates to an activation energy of 144.0 kJ/mol (±33.9, 1 s.e.).

4. DISCUSSION

4.1. Catalysis on reactor surfaces?

Experiments were conducted in gold cells with passivated titanium heads. One concern is that these surfaces may provide catalytic sites that promote C-H activation and thus catalyze methane hydrogen isotope exchange reactions. We evaluate this here before interpreting the data further. The gold was chosen because it is both flexible and is generally considered to be chemically inert. However, we note that C-H activation of long chain linear alkanes ($>C_{20}$) has been observed on gold (Zhong et al., 2011), and trace impurities of Fe in commercial gold have been proposed to catalyze methane generation from acetate (Lazar et al., 2015). But, we are unaware of any evidence that gold catalyzes C-H activation in methane to promote isotope exchange with water. Alternatively, the titanium head, despite being passivated, could also act as a catalyst for hydrogen isotope exchange. In any of these cases (catalysis on gold, impurities, or titanium), the hydrogen isotope exchange rate would be a function of the total amount of methane in the experiment relative to the exposed surface area of the gold cell or titanium head. The data is not consistent with such catalysis. Specifically, catalysis on the gold or titanium head would not yield constant determined values for k_r in an experiment (i.e., linear slopes over hundreds of days as in Fig. 2). This is because, as we sample, we remove experimental fluid and reduce the cell volume, lowering the total moles of methane in the experiment (though the concentration is kept constant), while the surface area of the gold and titanium remains constant. Over the course of an experiment, fluid volumes are typically reduced by 2–3× relative to the starting fluid volume, increasing the ratio of the gold or titanium surface area to methane content by an equivalent factor. We would expect such a change would increase rates of catalysis by similar amounts (which would result in the plots in Fig. 2 curving concave downwards as opposed to being straight). As this is not observed, we propose and proceed with the assumption that catalysis on the gold cell or titanium head is not driving the observed changes in methane δD. Rather, we propose that we have determined uncatalyzed exchange rates for hydrogen isotopes between dissolved methane and a fluid comparable to liquid water. We consider our exchange rates comparable to that in liquid water because the supercritical fluids in the experiments have a density of ∼0.58 g/ml, which is above the critical density of pure water (0.322 g/ml).

4.2. Comparison to previous kinetic determinations

As discussed in the introduction, there are two studies that have been used to infer the rate of hydrogen isotope exchange between methane and liquid water: Reeves et al. (2012) at 323 °C and Koepp (1978) at 200 °C. As these experiments have been used to calculate timescales for methane hydrogen isotope equilibration with liquid water in a variety of recent studies as a function of temperature (e.g., Wang et al., 2018; Beaudry et al., 2021; Xie et al., 2021), we review them in detail and compare these prior results to our determinations.

Reeves et al. (2012) sampled methane (and other alkane gases) dissolved in liquid water at 323 °C as a function of time. Two experiments were conducted and in one experiment the δD of the water was purposely changed in the middle of the run such that there are effectively three separate experiments with which one can estimate rates of hydrogen isotope exchange between methane and liquid water. Similar to our study, these experiments were con-

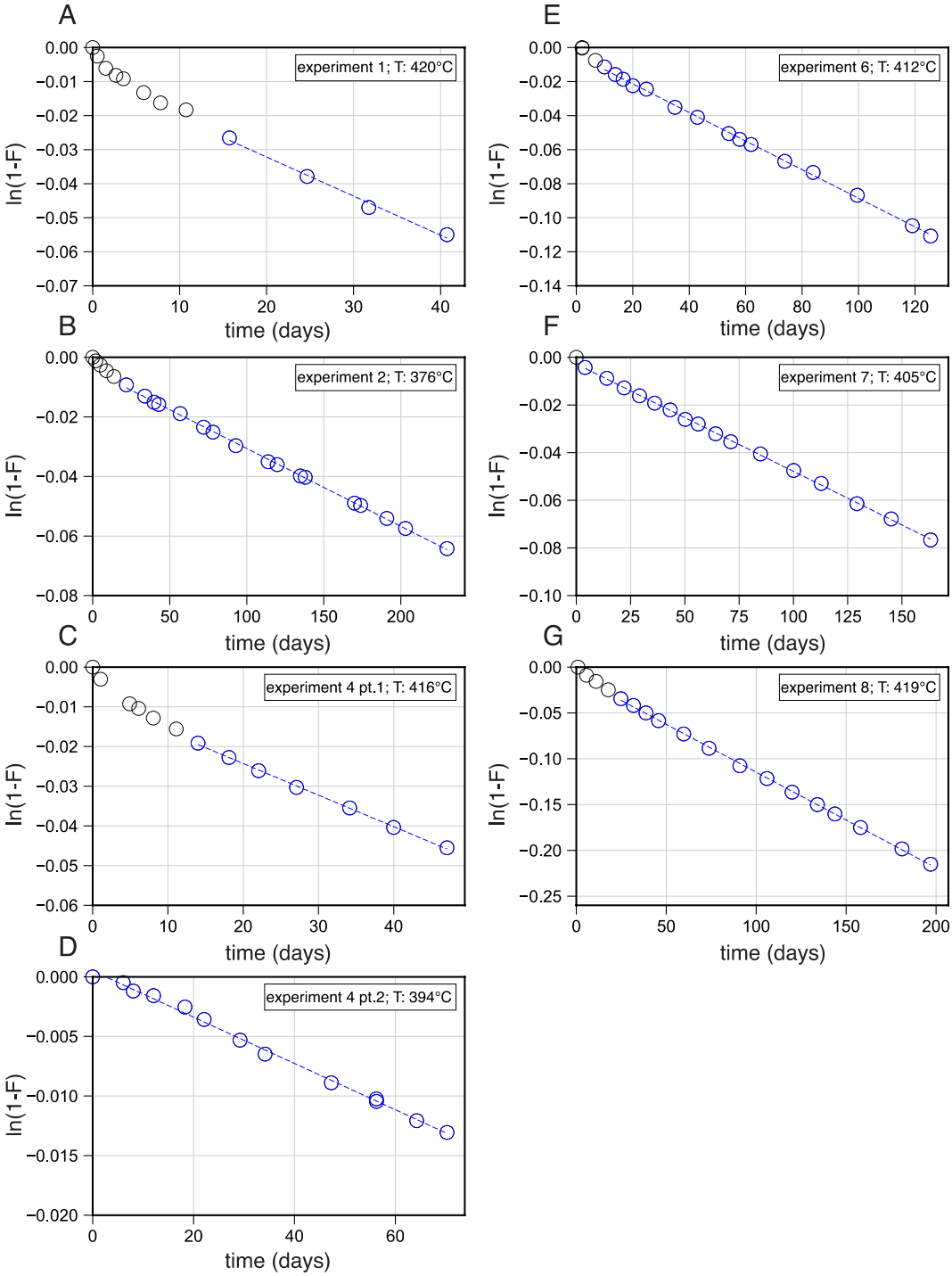

Fig. 2. Plots of ln(1 − F) vs. time (days) for all experiments used in calculation of k_r in this study. Blue dotted line is a linear regression of the selected points. Blue points are included in the regression and black points are excluded. ±1σ error bars are smaller than the size of the point in all cases.

ducted using a flexible gold cell system. However, unlike our experiments, pyrite, pyrrhotite, and magnetite were included to both buffer redox conditions and minimize alkane oxidation, and ethane, propane, *n*-butane, and *n*-pentane were simultaneously reacted along with the methane. Experiments were run for similar extents of time as here (up to ~200 days). Maximum fractional approaches to hydrogen isotope equilibrium for methane were 6%. As discussed in the *Introduction*, Reeves et al. (2012) did not attempt to calculate a rate constant for hydrogen isotope exchange between methane and liquid water based on their experimental data.

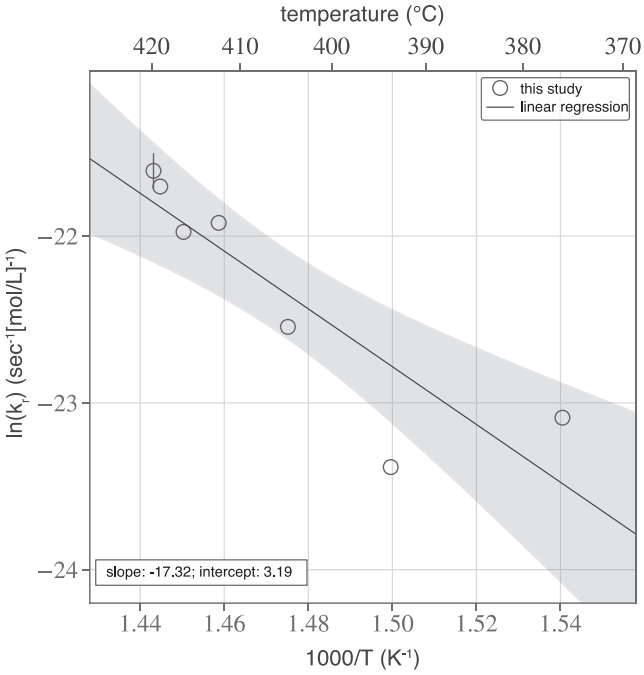

Fig. 3. Plot of $\ln(k_r)$ ($\ln(sec^{-1}\,[mol/L]^{-1})$) vs. 1000/T ($K^{-1}$) from our experiments. Shading represents the 95% confidence interval. Error bars are $\pm 1\sigma$; when smaller than the size of the point, they are not shown. Activation energy calculated from this regression is 144.0 ± 33.9 kJ/mol.

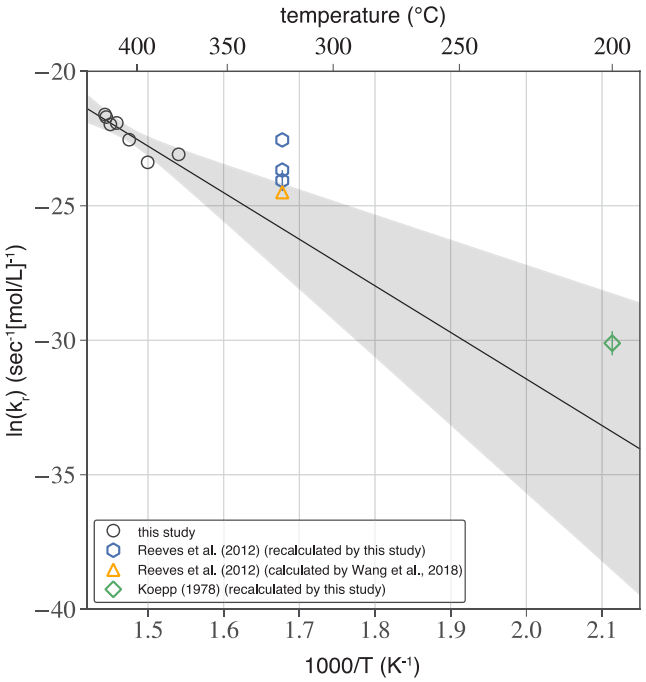

Fig. 4. Plot of $\ln(k_r)$ ($\ln(sec^{-1}\,[mol/L]^{-1})$) vs. 1000/T ($K^{-1}$) based on our data as compared to data from Koepp (1978) and Reeves et al. (2012) as calculated by this study and by Wang et al. (2018). The recalculated point by Wang et al. (2018) is for their 'best guess' 24 year 50% equilibration time and corrected for the density of water as discussed here. Shading represents the 95% confidence interval associated with the regression. Error bars (1σ) for data from this study are all smaller than the point and are not shown. For Reeves et al. (2012), error bars are ± 1 s.e.; when smaller than the size of the point, they are not shown. This error is based on the ± 1 s.e. of the regression slope. For Koepp (1978), the error bar is the estimated $\pm 1\sigma$ uncertainty based on the Monte Carlo calculation discussed in the text.

Under the assumption that hydrogen exchange between methane and water caused the methane δD shift in the Reeves et al. (2012) data, Wang et al. (2018) provided visual comparisons to the experimental data for values for $k_r[H_2O]$ vs. time at 323 °C based on timescales to reach 50% equilibration of 6, 12, and 24 years. The value for 24 years was presented as their preferred 'best-guess' estimate that best visually fit the Reeves et al. (2012) experiments. They did not convert these to values of k_r. These 50% equilibration timescales (6–24 years) are equivalent to a range for $k_r[H_2O]$ of 3.66×10^{-9} to 9.16×10^{-10} sec^{-1}. Based on the conditions given in Reeves et al. (2012), the density of water in their experiments was 0.718 g/ml. As such, these $k_r[H_2O]$ values correspond to values for k_r of 9.19×10^{-11} to 2.3×10^{-11} sec^{-1} $[mol/L]^{-1}$.

We additionally formally fit the data of Reeves et al. (2012) using our calibration of the temperature dependence of hydrogen isotopic equilibrium between methane and water (Eq. (3)). We note that at 323 °C, this yields a value of $1000 \times \ln{}^{D}\alpha_{CH4(g)\text{-}H2O(l/sc)}$ of −114.1‰ vs. the value used in Wang et al. (2018) of −139.3‰. We plot ln(1 − F) vs. time for the Reeves et al. (2012) data in Fig. A3. Based on our regressions of the three experiments from Reeves et al. (2012), we calculate values for k_r of between to 3.55×10^{-11} to 16.06×10^{-11} sec^{-1} $[mol/L]^{-1}$. These overlap with the visually estimated range given in Wang et al. (2018) (2.3×10^{-11} to 9.19×10^{-11} sec^{-1} $[mol/L]^{-1}$, see above). Using the best-guess estimate of Wang et al. (2018) for a 50% equilibration timescale of 24 years yields a difference in k_r vs. the extrapolated value from our experiments of 3.9× (or 1.4 natural log units). For comparison, our calibration predicts that at 323 °C, the value for k_r would be 0.59×10^{-11} sec^{-1} $[mol/L]^{-1}$ with an extrapolated ±2 standard deviation (σ range of between 0.11×10^{-11} and 3.20×10^{-11} sec^{-1} $[mol/L]^{-1}$) and thus lower beyond ±2σ compared to various estimates derived from our fits to the Reeves et al. (2012) data (Fig. 4). We consider the above differences to indicate relatively good agreement between the various studies given the different experimental conditions and, as acknowledged by Wang et al. (2018), the high uncertainty involved in calculating rate constants from the Reeves et al. (2012) data. Alternatively, the potentially elevated rates from Reeves et al. (2012) could be real and due either to synthesis of new methane in their experiments or due to catalysis on the minerals (pyrite, pyrrhotite, and magnetite) present in their experiments.

The second constraint used to estimate hydrogen isotope exchange rates between methane and water is from Koepp (1978) at 200 °C. This study is an abstract and it describes an experiment where methane was reacted with D_2O in a stainless-steel vessel. Koepp (1978) provides three estimates for the exchange rate between methane and water (specifically $k_r[H_2O]$) in a base-10 log-scale bar graph at 100, 200, and 240 °C (Fig. 1 of that work). No experimental data is given, nor detailed methods described. It is important to note that the only point that was experimentally determined is the 200 °C point—the 240 °C and 100 °C values were calculated using an assumed activation energy for hydrogen isotope exchange based on experiments of Watt et al. (1966) in which gaseous D_2 and CH_4 were reacted at temperatures ranging 1167–1482 °C. Although it is not explicitly stated in the abstract what phase(s) of water was present during the experiment, the Koepp (1978) study is commonly assumed to constrain exchange between dissolved methane and liquid water. As a result, the Koepp (1978) results have been used in one of two ways. First, the $k_r[H_2O]$ value given at 200 °C and those calculated at 100 °C and 240 °C have been used (as reported) to estimate the isotope exchange rate between methane and water at a variety of temperatures (e.g., Xie et al., 2021). Alternatively, Wang et al. (2018) combined the estimate at 200 °C from Koepp (1978) with an estimate at 323 °C using the Reeves et al. (2012) data (best-guess estimate described above) to determine the temperature dependent rate of methane-liquid water hydrogen isotope exchange. The equation for this calibration is provided in Beaudry et al. (2021) and was further used in that study to estimate hydrogen isotope exchange rates in terrestrial hydrothermal systems. We note that neither relationship was corrected for potential differences in water density between the experiments and thus cannot be straightforwardly compared to each other or our experiments here—this is especially true for the Koepp (1978) experiment where the phase of water is not known (as expanded on below).

Given the recent use of the Koepp (1978) abstract for anchoring exchange rates of methane with liquid water at geologically relevant conditions, we obtained the original reports on which this abstract is based (Köpp, 1977, 1978; note that Koepp and Köpp are different spellings of the same name). Based on the methods provided (Köpp, 1977), reactions were conducted in a stainless-steel cylinder with 150 ml of reaction volume. Before heating, 2 ml of 99.7% D_2O were added, the system pressurized with 30–40 bar CH_4, and then heated to 200 °C. Based on the model of Duan and Mao (2006), under these conditions, >99.9% of the methane would be in the gas phase and a two-phase system would exist with ~1 ml of D_2O remaining in the liquid phase. Thus the Koepp (1978) experiment, as described, occurred in a two-phase system with the methane dominantly in the gas phase. As such, use of this experiment as a constraint on exchange rates for dissolved methane in liquid water is not straightforward. Additionally, the degree of observed exchange is small: the rate constant derived is from a total δD_{CH4} change of 9‰ (±3.6‰, 1σ) from the initial methane vs. a single time point sampled at 400 days. This corresponds to a fractional approach to isotopic equilibrium of 0.0001%.

Given the above discussion, we do not consider the experiment of Koepp (1978) to provide clear constraints on the exchange rates between methane and liquid water at 200 °C. We compare this data point to our data by assuming the exchange occurred mostly in the gas phase and divide the calculated $k_r[H_2O]$ by the concentration of D_2O in the gas phase at steam saturation (0.435 mol/L at 200 °C). This yields a value for k_r of 8.39×10^{-14} (sec^{-1} $[mol/L]^{-1}$; $\pm 3.76 \times 10^{-14}$, 1σ) The uncertainty was calculated using a Monte Carlo approach by incorporating the stated uncertainty of the δD of the initial and final methane (assumed to be ±1σ). We calculated the rate constant one million times by varying the starting and final methane

assuming a Gaussian distribution based on the $\pm 1\sigma$ uncertainty. If we extrapolate our rate to 200 °C based on the best-fit line given (Eq. (5)), we obtain a value for k_r of 0.31×10^{-14} (sec^{-1} $[mol/L]^{-1}$) with an extrapolated $\pm 2\sigma$ range of between 58.2×10^{-14} to 0.002×10^{-14} (sec^{-1} $[mol/L]^{-1}$). As such, the two agree within 2σ, differing on average by 27.0× or 3.3 natural log units. Considering the large amount of extrapolation and very different experimental conditions, we consider this level of agreement to be surprisingly good.

In Fig. 4 we extend the regression of our data and the associated 95% confidence interval (shown in Fig. 3) to lower temperatures, comparing our results to the rates derived from the other two experimental studies. Despite similarities between our extrapolation and prior results, we do not use them in our regression. We do not use the Koepp (1978) data as we consider it unclear the actual conditions of the reaction (e.g., is the exchange occurring in the gas phase, liquid phase, or both). We exclude the rate derived from Reeves et al. (2012) because the experiments are different from those presented here, having included potentially catalytic minerals. We additionally note that the catalytic properties of the steel reactor used in Koepp (1978) are unknown.

4.3. Implications for environmental methane

A common way to represent the conditions under which isotope exchange between species or phases occurs is to calculate the time required at a given temperature for measurable exchange to occur or, alternatively, the temperature below which exchange is negligible (e.g., Zhang, 2008). The temperatures at which isotopic exchange begins proceeding during warming or stops during cooling is often termed a 'blocking' or 'closure temperature' (e.g., Zhang, 2008). This is an inexact term as it is a function not only of the temperature, but also the time-temperature history of the sample. The blocking temperature for hydrogen isotope exchange between methane and either itself or with other hydrogen-bearing species such as liquid water is uncertain. For example, Burruss and Laughrey (2010) proposed that methane and water begin exchanging hydrogen isotopes in sedimentary systems at temperatures between 250 and 300 °C. Based on methane clumped-isotope temperatures and differences in δD of methane vs. water in fluid inclusions in quartz, Mangenot et al. (2021) proposed that hydrogen isotope equilibration between methane and water does not occur on geologic timescales (i.e., at cooling rates during sedimentary uplift; e.g., of order 10 °C/myr) at temperatures below ~300 °C. Finally, based on clumped-isotope temperatures from several marine hydrothermal vent sites, Wang et al. (2018) proposed that closure temperatures are between 270 and 360 °C for hydrogen isotope exchange between methane and water in hydrothermal systems. In contrast, Labidi et al. (2020) proposed that measurable hydrogen exchange between methane isotopologues can occur at temperatures as low 65 °C during conductive cooling of fluids in some hydrothermal systems. Similarly, Giunta et al. (2021) proposed that in sedimentary systems, methane isotopologues can equilibrate via hydrogen isotope exchange reactions at temperatures as low 90 °C. In the latter two cases, whether this proposed exchange process involves liquid water or not is uncertain.

Our results allow us to calculate the timescales required for measurable hydrogen isotope exchange to occur between methane and liquid water and thus evaluate what process may or may not be occurring in the systems identified above for defined time-temperature paths. To do this, we provide the time required at a given temperature for some degree of reaction to occur (Fig. 5)—similar sorts of estimates for this based on the results from Reeves et al. (2012) and/or Koepp (1978) are given in Wang et al. (2018) and Xie et al. (2021). In Fig. 5, as a guide, we provide as a filled color band the timescale for 1–99% equilibration with a solid line for 50% equilibration. In doing this, we assume the density of water is 1 g/ml, which approximates expected rate maxima at any given temperature (as water density is typically equal to or lower than 1 g/ml under environmental conditions). Values outside of 420–376 °C are an extrapolation of Eq. (5) and thus beyond the calibrated range.

Before discussing this figure, it is important to note that this extrapolation carries significant uncertainty beyond the uncertainty calculated in the regression used to derive Eq. (5). For example, we do not know the chemical mechanism driving the observed isotope exchange reactions in any of the experiments. As such, mechanisms may change as a function of temperature such that different reaction pathways are dominant at different temperatures. We note that Beaudry et al. (2021) proposed that the exchange proceeds by an $H^{\cdot}$ radical reacting with CH_4 to form a $CH_3^{\cdot}$ radical that then abstracts H from H_2O. If correct, then the key process controlling the rate of exchange is $H^{\cdot}$ radical generation to initiate the formation of $CH_3^{\cdot}$. They further proposed that $HS^{\cdot}$ radicals could also promote H abstraction from CH_4. Finally, the physical properties of water vary as a function of temperature (e.g., the dielectric and dissociation constants) and such changes may alter rates at lower or higher temperatures. Given this uncertainty, some caution should be taken in this extrapolation. Nevertheless, we consider it a useful starting point in terms of considering environmental data.

We also provide in Fig. 5 the timescale for hydrogen isotope equilibration if methane were to react with water vapor. We calculated these rates using the density of pure water vapor along the steam saturation curve to the critical point (374 °C). In doing this we are using the activation energy and prefactor (i.e., Eq. (5)) derived from exchange between dissolved methane and liquid water and we are assuming that water vapor concentrations are sufficiently high relative to methane that only the δD of methane changes measurably. In doing this, we are effectively assuming that hydrogen isotope exchange rates between methane and water are proportional to the collisional frequency between molecules and that solvation effects for isotope exchange reactions in liquid vs. gaseous systems are unimportant. This is likely incorrect. Regardless, this comparison serves mostly to illustrate that large changes in rates may accompany the phase transition from liquid to gaseous

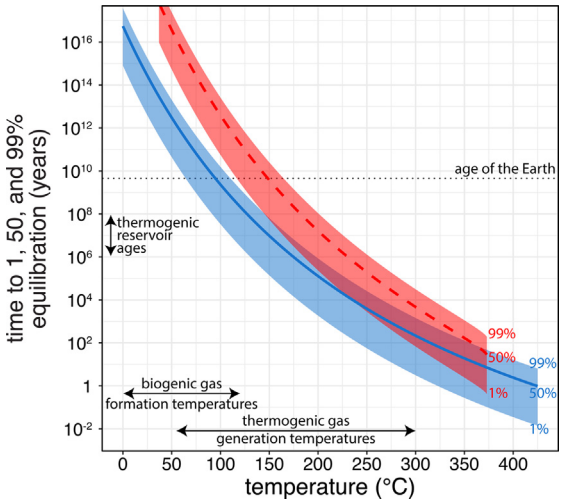

Fig. 5. Calculations of timescale for the fractional equilibration of the hydrogen isotopic composition of methane and liquid/supercritical water (blue) or water vapor (red) based on Eqs. (4) and (5). Shaded regions are for 1–99% fractional equilibration. The lines are for 50% equilibration. For liquid/supercritical fluids, the density is taken as 1 g/ml. Thus the rates represent likely maximum rates as water density in high-temperature (>300 °C) hydrothermal systems is typically lower that 1 g/ml. For vapor, the density of pure water at steam saturation is used. Water density at the critical point (374 °C) is ~0.322 g/ml (rate ~3× slower than unit density curve in blue at the same temperature). Relative changes in vapor density with temperature are more substantial, for example, 0.114, 0.008 and 0.0006 g/ml at 350 °C, 200 °C and 100 °C, respectively.

systems solely due to the difference in water density. We note that the assumption that second-order rate constants for hydrogen isotope exchange scale mostly with the density of the water has been shown to be consistent with rates of H_2-H_2O hydrogen isotope equilibration in gaseous and liquid systems (Pester et al., 2018).

In Fig. 5 we see that at temperatures less than ~125 °C, the timescale to reach 50% hydrogen-isotope equilibration between methane and liquid water takes >100 million years and over a billion years below 100 °C. This indicates, for our extrapolated kinetics, that abiotic, uncatalyzed hydrogen isotope exchange between methane and liquid water should not occur on geologic timescales at these low temperatures. From 125 to 200 °C, exchange is predicted to take place at timescales of hundreds of millions to hundreds of thousands of years. Timescales for exchange are order hundreds of years at 300 °C and of order one year at 400 °C. With these patterns in mind, we first consider the implications of these results for methane originating from low-temperature sedimentary systems (<125 °C), followed by warmer temperature thermogenic systems (~125–250 °C), and then deep-sea hydrothermal systems.

4.3.1. Low-temperature sedimentary systems

Eq. (5) indicates that the timescales for 50% equilibration for hydrogen isotope exchange between methane and liquid water are greater than the age of the Earth at temperatures less than 95 °C (>5 billion years, Fig. 5). However, hydrogen isotope exchange between methane and water is thought to occur at temperatures as low as ~0 °C in microbially influenced systems. This is based on the observation that in many sedimentary systems, differences between the δD of methane and water as well as measured methane clumped-isotope compositions are consistent with the methane forming in or later attaining hydrogen isotopic equilibrium with water (Stolper et al., 2015; Wang et al., 2015; Douglas et al., 2016, 2017; Okumura et al., 2016; Ijiri et al., 2018; Gropp et al., 2021; Jautzy et al., 2021; Turner et al., 2021). This equilibration has been proposed to be facilitated by methanogenic or anaerobic methanotrophic organisms whose enzymes catalyze the exchange of hydrogen isotopes between methane and water (Stolper et al., 2015; Wang et al., 2015; Douglas et al., 2016; Okumura et al., 2016; Gropp et al., 2021; Jautzy et al., 2021; Ono et al., 2021; Turner et al., 2021; Wegener et al., 2021). Thus, in low-temperature systems where biology is active, rates of hydrogen isotope exchange between methane and water are enhanced by factors on the order of billions over abiotic rates. As such, equilibration of hydrogen isotopes between methane and liquid water from low-temperature systems could potentially be used as a biomarker on Earth and perhaps other planetary bodies where methane is found. This requires that other processes such as catalysis on mineral surfaces are too sluggish to equilibrate the hydrogen isotopes of methane and water at low temperatures (<100 °C) on geological timescales—such is not yet known.

We note that methane samples from the Kidd Creek Mine (Canada) may support such sluggishness even when minerals are present. Specifically, fluids in this system have been isolated for hundreds of millions to ~2 billion years (Warr et al., 2018) and today are at low temperatures (<65 °C; Sherwood Lollar et al., 2008). Methane emitted from these systems have δD values that are out of hydrogen isotope equilibrium by hundreds of per mil with respect to co-associated waters, which has been interpreted to indicate that hydrogen isotope exchange did not occur significantly following methane formation (which is proposed to be via

abiogenic processes; Sherwood Lollar et al., 2008; Reeves et al., 2012). If this methane formed hundreds of millions of years ago, it would support our model's prediction that at low temperatures (<100 °C) equilibration does not occur even on long (billion year) geologic timescales and thus that mineral-catalyzed hydrogen isotope exchange between methane and water is not significant in some geologic systems.

4.3.2. Thermogenic methane

Thermogenic gases are typically thought to be generated from about 60 to 300 °C (Quigley and Mackenzie, 1988; Hunt, 1996; Seewald, 2003) and liquid water is commonly invoked to play a role in the chemical reactions that both govern the generation of liquid and gaseous hydrocarbons, and set their hydrogen isotopic composition (Hoering, 1984; Lewan, 1997; Seewald et al., 1998; Seewald, 2003; Schimmelmann et al., 2006). Based on the kinetics determined here, if methane is retained and exposed to liquid water for tens of millions of years at 150 °C or hundreds of thousands of years at 200 °C, then the methane could equilibrate its hydrogen isotopic composition with any liquid water that is present before being expelled and trapped at a shallower and cooler depth (Fig. 5). This scenario would require that rates of gas generation are sufficiently slow in a given system such that gas that forms is retained in the source rock for sufficiently long to equilibrate with associated waters prior to primary expulsion and subsequent migration. Timescales of gas generation, accumulation, and migration will be set by the temperature-dependent kinetics of gas generation of a given organic source, burial rate (and thus heating rate) of a system, and overall storage capacity of the formational rock for hydrocarbons before expulsion occurs (e.g., Sandvik et al., 1992; Pepper and Corvi, 1995).

Following expulsion, such equilibrated gases could then migrate to a shallower and cooler reservoir where kinetics would be slower. If the reservoir is gas dominated, then water may be in the vapor phase, which, at 150 °C, would require billions of years to equilibrate the isotopes of methane and water (Fig. 5). Alternatively, the gas could migrate and then dissolve in liquid hydrocarbons in an oil-dominated reservoir. In such a system water is not the solvent and thus will be at a lower activity in the oil as compared to a water-dominated system and would limit the rate of isotope exchange between water and methane. In either case, the hydrogen and clumped isotopic composition of the methane could reflect the formation and initial storage temperature of the methane before expulsion and migration to lower temperatures.

Such a pathway may explain the observation that thermogenic gases from high-maturity source rocks (vitrinite reflectance [R_o] > 1.7%—equivalent to >170 °C max burial temperatures) commonly yield methane in clumped isotope equilibrium (e.g., Stolper et al., 2014a, b; Wang et al., 2015; Young et al., 2017; Eldridge et al., 2019; Giunta et al., 2019), while lower maturity gases show kinetic isotope effects (Shuai et al., 2018; Stolper et al., 2018; Xie et al., 2021). How this equilibrium is reached remains uncertain, with proposals including equilibration with water, on minerals, or via radical reactions (Stolper et al., 2014a, 2018; Dong et al., 2021; Xie et al., 2021). Based on the hydrogen isotope exchange rates calculated here, such equilibration could occur during gas generation above ~150 °C with liquid water present and then be frozen in once the gas migrates to lower temperatures or water-poor systems. We note that many of the systems studied are from unconventional systems in which the gas is retained in source rock (i.e., it has not migrated out of the system). Methane in such systems may be particularly susceptible to isotope exchange reactions with water as gas is retained in its formational environment and cools more slowly during uplift vs. more rapid migration and cooling to a reservoir. This assumes that exchange rates between methane and other hydrocarbons is slower than exchange with liquid water. A similar inference was made by Xie et al. (2021), but based the kinetics given in Koepp (1978) at 200 °C and their assumed activation energy.

Recent measurements of thermogenic gases trapped in inclusions from the Swiss orogenic thrust belt provide data that constrain apparent closure temperatures for methane isotopologues reacting with water (Mangenot et al., 2021). Specifically, in this system, methane was trapped either as a separate bubble in an inclusion with liquid water or inclusions that are mostly methane with liquid water present as a rind. Based on the homogenization temperatures of the inclusions, methane and water in the 'zone B' samples are thought to have been trapped at elevated temperatures (>200 °C), and then uplifted to the surface. Based on $^{13}CH_3D$ apparent temperatures from these inclusions, Mangenot et al. (2021) proposed that the closure temperature for hydrogen isotope exchange either between both methane isotopologues only and between methane isotopologues and water is greater than 250–280 °C.

We compared our predicted rates of hydrogen isotope exchange to these data. To do this we assumed the following: an invariant liquid water δD in the inclusions of −45‰ (average of reported inclusions in zone B), that methane starts with clumped-isotope temperatures of 250 °C (similar to the mean $^{13}CH_3D$-based temperature of 244 °C) and δD_{CH4} of −130.2‰ (zone B average). For the geologic history, we assumed uplift occurred over 15 million years at a constant rate to a final temperature of 25 °C (based on geologic histories given in Mangenot et al., 2021). We used the kinetics for hydrogen isotope exchange with liquid water assuming a water density of 1 g/ml. We derive in the appendix a model for rates of change of the isotopologue $^{13}CH_3D$ with water and show that, if we assume no kinetic isotope effects associated with exchange of hydrogen or deuterium for a ^{12}C vs. ^{13}C bearing isotopologue, that relative rates of exchange for $^{12}CH_3D$ and $^{13}CH_3D$ with water are identical. Details of the forward model are given in Appendix A2. This simulated thermal history yields methane δD and $^{13}CH_3D$-based temperatures significantly different from what is contained in the inclusions: δD_{CH4} are predicted to be −162.2‰ (vs. −130.2‰) and $^{13}CH_3D$-based temperatures are calculated to be 176 °C vs. the mean average temperature for zone B gases of 244 °C (±8 °C, 1σ). Consequently, these samples and our kinetic data do not match, with our kinetic data predicting faster-than-observed rates of exchange.

This mismatch is not surprising as the modeling above assumes methane is dissolved in liquid water during the entire thermal history, which is not the case for these samples. This is because currently at ambient temperature two phases coexist in the inclusions. As noted above, one population of inclusions contains mostly fluid methane with water existing only as a liquid rind, and another population is water rich with an immiscible methane fluid bubble. As such, in both inclusions, methane has either not been dissolved in water (fluid methane with a water rind) or underwent a phase separation during cooling (the methane bubble inclusions in water) over the complete the geologic history of the inclusions. Consequently, the concentration of water in the methane rich portions of these systems may have been sufficiently low to significantly slow down rates of exchange with the water compared to our analysis above. This demonstrates that there is unlikely to be a single closure/blocking temperature for hydrogen isotope exchange between methane and liquid water, and that it will depend not only on the thermal history but also on the phases present and their water activities.

4.3.3. High-temperature hydrothermal systems

The experimental data presented here are particularly relevant to high-temperature hydrothermal and geothermal systems where methane is dissolved in liquid and supercritical water as the experimental temperatures directly overlap temperatures observed in these systems. Here we focus on fluids from oceanic hydrothermal systems where the δD of the methane has previously been used to constrain gas origins (Horibe and Craig, 1995; Proskurowski et al., 2006; Wang et al., 2018; Labidi et al., 2020). We note that Beaudry et al. (2021) has recently presented results on the isotopic composition of methane from terrestrial geothermal systems. They compared their results to isotope exchange rates calculated from the Koepp (1978) and Reeves et al. (2012) experiments based on the temperature dependence for $k_r[H_2O]$ given in Wang et al. (2018). They perform similar sorts of calculations as done here and we refer the reader to that study for an examination of terrestrial geothermal systems.

Deep-sea hydrothermal solutions exit the seafloor at temperatures as high as ~405 °C when directly measured using thermocouple probes (e.g., Von Damm et al., 2003; McDermott et al., 2018) at which point the fluids are rapidly cooled to lower temperatures via mixing with seawater. The origin of this methane remains an active area of inquiry with some proposals invoking methane generation in the active flow and others formation outside of the flow (as reviewed in McDermott et al., 2015). The stable clumped isotopic composition of methane has recently been used to test these formational pathways (Wang et al., 2015, Labidi et al., 2020). Based on differences between methane clumped-isotope temperatures (specifically $^{13}CH_3D$-based temperatures) and fluid emission temperatures, and the tendency of these $^{13}CH_3D$-based temperatures to be ~300 °C, Wang et al. (2018) proposed that methane in these hydrothermal systems neither forms in nor exchanges hydrogen isotopes with water in the actively circulating portions of the system. Rather, they proposed that the methane forms outside of the active hydrothermal system via reduction of CO_2 by H_2 where the H_2 was generated during serpentinization of igneous minerals. This has been proposed to occur in fluid inclusions in igneous minerals (Klein et al., 2019). The idea is that during or following formation, the methane isotopically equilibrates to ~300 °C with seawater-derived fluids in the inclusions prior to being entrained in the active flow and emitted to the ocean. Attainment of isotopic equilibrium in the vent fluid methane is supported by the observation that in all systems except Lost City (discussed below), $^{13}CH_3D$- and $^{12}CH_2D_2$-based temperatures yield overlapping values (Labidi et al., 2020). However, as Labidi et al. (2020) notes, re-equilibration could occur in the carrier fluid during active venting depending on the rates of hydrogen isotope exchange for methane.

In the Lost City system, $^{13}CH_3D$- and $^{12}CH_2D_2$ based temperatures do not overlap and this methane has been proposed to have partially re-equilibrated during upflow. What exact chemical reaction promotes the exchange was not known, but exchange with water or direct exchange between methane isotopologues were suggested (Labidi et al., 2020). Lost City has lower exit temperatures than other systems (<100 °C vs. >200 °C for end-member fluids) and different mineral assemblages associated with the vents (e.g., carbonate chimneys) and therefore reactions promoting hydrogen isotope exchange may differ compared to more typical marine hydrothermal systems as will be discussed below. Finally, Wang et al (2018), noted that the clumped isotope constraints from their study are limited to vents systems from slow-spreading ridges (specifically Lost City, Von Damm, Lucky Strike and Rainbow, as are those from Labidi et al., 2020). They proposed, though, that their model for methane formation may also apply to faster spreading systems.

Wang et al.'s (2018) model for methane formation is predicated on the assumption that the hydrogen (including clumped) isotopic composition of methane reflects conditions in which methane reached isotopic equilibrium outside of the active flow (e.g., in a fluid inclusion), internally and with seawater derived fluids, and that after entrainment in the active flow, the isotopic composition did not change. The following must be true for this to be correct: First, either methane has to form in isotopic equilibrium or must be sequestered in inclusions for a sufficiently long period of time that the methane reaches hydrogen isotopic equilibrium with local fluids and internal clumped isotopic equilibrium. Second, following entrainment in the fluid, any warming or cooling must occur on timescales too short to modify the isotopic composition of the methane.

We can examine these requirements quantitatively using our experimentally determined rates. To do this, we divide the thermal history of methane in deep-sea hydrothermal systems into three stages starting with the last process to occur and stepping back in time: (*i*) Final ascent and cooling of the fluid as it is vented to the seafloor; (*ii*) Time at peak temperature in the active hydrothermal system before ascent and cooling; (*iii*) Time required to equilibrate to ~300 °C before entrainment in the active flow. In all kinetic

calculations we assume that isotopologues of methane only exchange hydrogen isotopes with water rather than with each other. Our basis is that water is the dominant hydrogen-bearing species in these systems (generally there is ~10,000× more H in water than CH_4 in hydrothermal systems)—such has been assumed previously (Wang et al., 2018; Beaudry et al., 2021; Xie et al., 2021), though we note that Giunta et al. (2021) proposed that hydrogen isotope exchange between methane isotopologues could proceed at different rates as compared to hydrogen isotope exchange between methane and water in some environmental systems. We note our discussion excludes data from hydrothermal systems in which the methane is thought to be derived from the thermal breakdown of organic matter in sediments (e.g., from Guaymas Basin (Wang et al., 2015) and Juan de Fuca ridge (Douglas et al., 2017)) as the formational pathways of this methane are distinct from methane likely generated by reduction of CO_2 in the systems described above.

(i) Final ascent and cooling: We first quantitatively examine the isotopic impacts on methane of cooling of hydrothermal fluids as they ascend to seafloor. To explore this, we assume methane starts in both clumped equilibrium and hydrogen isotopic equilibrium with fluids at 300 °C—this temperature is the approximate average $^{13}CH_3D$ temperature of a range of hydrothermal samples in Wang et al. (2018)—they specifically found a mean temperature of 310 °C while Labidi et al. (2020) found a mean temperature of ~330 °C. We use 300 °C for simplicity. This temperature (~300 °C) was assumed by both Wang et al. (2018) and Labidi et al. (2020) to be representative of the typical initial equilibration temperature of methane emitted from marine hydrothermal systems—note, as discussed above, that this temperature reflects a condition in which methane reached internal isotopic equilibrium was confirmed by Labidi et al. (2020) through demonstration of overlapping $^{13}CH_3D$- and $^{12}CH_2D_2$-based temperatures on the same gases examined by Wang et al. (2018). We additionally assume the water has a constant δD_{H2O} of 0‰ (i.e., seawater). We then assume the fluid is instantaneously heated to 400, 450, or 500 °C before cooling during ascent to the seafloor to 0 °C. We allow for these elevated temperatures compared to the exit temperatures as chemical geothermometry studies indicate that minimum fluid temperatures deeper in hydrothermal systems are commonly 50–150 °C higher than exit temperatures (e.g., Foustoukos and Seyfried, 2007; Pester et al., 2011; Seyfried et al., 2015; Scheuermann et al., 2018). High-temperature (black-smoker) fluids are thought to ascend ~1 km in a matter of hours (Wilcock, 2004) during which time they conductively cool. These ascent rates equate to conductive cooling rates of ~50 °C/hr to the emission temperatures (typically ~350–370 °C) at the seafloor (Pester et al., 2018) followed by rapid cooling during mixing with cold seawater (~0 °C).

We compare the 50 °C/hr cooling rate given in Pester et al. (2018) with a rate 100× slower (0.5 °C/hr) in order to explore the importance of the chosen rate on the model results. For modeling ease, we assume cooling at these constant rates to temperatures of 0 °C rather than simulating the quenching process that occurs when hot vent fluid mixes with seawater—this simplification is unimportant as will be shown. Finally, to do these calculations, we must constrain the fluid density along the flow path, which requires estimating the associated hydrostatic pressure at each temperature. To do this, we use pressures and densities along the two-phase boundary of seawater (~3.2 wt.% NaCl) for temperatures >250 °C (Driesner and Heinrich, 2007; Driesner, 2007), and that of steam-saturated pure liquid H_2O for temperatures <250 °C where, for our purposes, the presence of salt has a negligible effect on the moles of H_2O per volume of solution (<1%). As an example, our assumed flow path affects partial molar (H_2O) densities of 40.6, 26.0, and 18.9 mol/L at 300, 400 and 500 °C, respectively, compared to 55.2 mol/L for bottom seawater (~4 °C).

Fig. 6A shows how the modeled δD of methane changes at different maximum temperatures and cooling rates. As seen, the modeled δD is effectively invariant regardless of cooling rate and starting temperature—i.e., all of the various thermal histories plot on top of each other and the maximum change in δD is 0.2‰. Systems where fluids may not have reached these high temperatures (e.g., Von Damm and Lost City) would change even less if they start cooling at lower initial temperatures (<400 °C). This limited change in δD_{CH4} is due to both the slow kinetics of exchange over the timescales used (hours to ~1 month) and the fact that the equilibrium hydrogen isotope fractionation between gaseous methane and liquid/supercritical water has a limited temperature dependence between 300 °C and 500 °C ($1000 \times \ln^{D}\alpha_{CH4\text{-}H2O(l/sc)}$ varies by less than 14‰ over this temperature range). For comparison, the δD of hydrothermal methane samples is plotted versus the measured exit temperatures (corrected for any entrainment of cold seawater). Except for samples from Lost City (discussed below), these data scatter around the equilibrium curve calculated at the fluid exit temperature and are largely consistent with methane preserving a relatively high formation temperature (>200 °C) and having reached hydrogen isotope equilibrium with seawater. However, as originally noted by Horibe and Craig (1995) and discussed by Wang et al. (2018), the temperature dependence of equilibrium hydrogen isotopic fractionation between methane and water is simply too small either for useful thermometry in these hydrothermal systems or to detect if isotopic exchange occurs during cooling to typical venting temperatures (>200 °C).

The clumped isotopes of methane provide a different way to examine rates of exchange in nature as, at equilibrium, their abundance versus a random distribution of isotopes is independent of the bulk isotopic composition (e.g., Eiler, 2007). We provide calculated $^{13}CH_3D$-based temperatures for the same cooling paths as above and compare environmental samples to these in Fig. 6B. In all cases, modeled $^{13}CH_3D$-based temperatures are not modified more than 3 °C regardless of cooling path or starting temperature. This shows that for the modeled thermal histories, exchange rates based on our experiments are too slow to change the isotopic composition of the methane during ascent and cooling, even if fluids are heated to as high as 500 °C prior to upflow. This is applicable regardless of

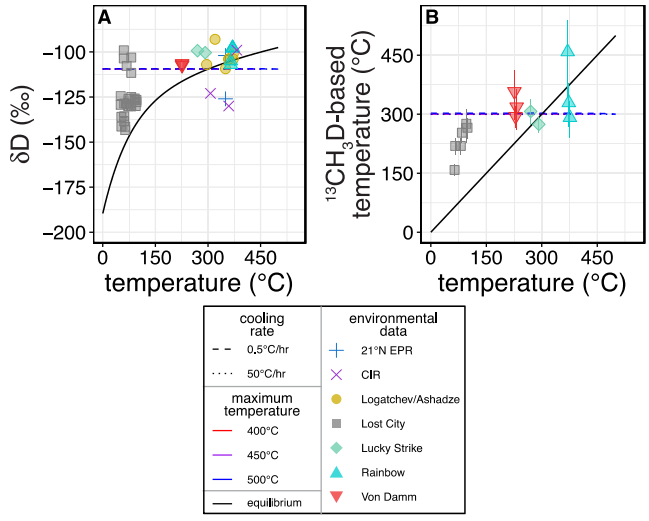

Fig. 6. (A) Calculation of changes in methane δD and (B) changes in $^{13}CH_3D$-based temperature for a system instantaneously heated from an isotopic composition in equilibrium with water ($\delta D_{H2O} = 0‰$) and internal clumped isotopic equilibrium at 300 °C to 400, 450, or 500 °C and then cooled at rates of 50 °C/hr or 0.5 °C/hr to 0 °C. This is done to simulate changes in the isotopic composition of methane during ascent and final venting in black-smoker systems during which fluids cool and are emitted to the seafloor. Note that all predicted paths effectively overlap one another. Environmental data (collected while venting to the seafloor) are plotted vs. maximum venting temperature (at seafloor) for end-member (unmixed) fluids. Data are from Horibe and Craig (1995), Proskurowski et al. (2006), Konn et al. (2015), Kawagucci et al. (2016), Wang et al. (2018), and Labidi et al. (2020). Note that in cases where Wang et al. (2018) and Labidi et al. (2020) measured the same samples, we used the values from Wang et al. (2018). EPR stands for East Pacific Rise while CIR stands for Central Indian Ridge. Error bars are ±1 s.e. or smaller than the size of the data point.

whether or not fluids experienced such high temperatures before cooling during upflow. Such is consistent when comparing fluids from the Rainbow and Von Damm vent fields that both preserve similar $^{13}CH_3D$ temperatures of ~300 °C despite venting at higher and lower temperatures, respectively (as originally observed by Wang et al., 2018). As such, our kinetic data support the hypothesis of Wang et al. (2018) that the hydrogen and clumped isotopic composition of methane are unlikely to be modified by exchange with water during ascent and cooling in high-temperature hydrothermal systems. This would indicate that the measured isotopic composition of the methane may reflect an earlier part of its thermal history.

Fig. 6 also shows that some Lost City methane samples have significantly lower δD values and lower $^{13}CH_3D$-based temperatures than observed in other hydrothermal systems. This is also consistent with lower $^{12}CH_2D_2$-based temperatures (see data in Labidi et al., 2020). Based on these differences, Labidi et al. (2020) proposed that at Lost City isotope exchange between methane isotopologues occurred during ascent to the seafloor and associated cooling to temperatures as low as 65 °C (Labidi et al., 2020). Although Labidi et al. (2020) focused on $^{12}CH_2D_2$ exchange, they proposed that $^{13}CH_3D$ compositions also changed from a starting $^{13}CH_3D$-based temperature of about 300 °C and re-equilibrated during cooling to an apparent $^{13}CH_3D$-based temperature as low as ~160 °C. They additionally noted that the δD of methane dissolved in the Lost City fluids is commonly depleted (−99 to −143‰) relative to the other high-temperature fluids they studied (−98 to −113‰), which would be consistent with hydrogen isotope exchange occurring between methane and water during cooling.

We compare our predictions for rates of exchange in the Lost City system vs. measured isotopic data. To do this, we assume (for simplicity) that methane starts in clumped isotopic equilibrium at 300 °C as above and in hydrogen isotopic equilibrium with water at 300 °C having a δD_{H2O} of 4‰ (the midpoint of the range for Lost City given in Proskurowski et al. (2006), which we keep constant). We then use the thermal history for Lost City fluids from Pester et al. (2018) in which samples start at 250 °C and cool at a rate of 0.4 °C/hr to a final temperature of 0 °C. We use the same water density vs. temperature relationship as used for the hydrothermal systems above.

This cooling rate predicts no measurable change in the isotopic composition of methane should occur during ascent and cooling of vented fluids at Lost City (δD is predicted to change by <0.000003‰ and $^{13}CH_3D$-based temperatures by <0.00005 °C). Attainment of a measurable change in the $^{13}CH_3D$ compositions observed (i.e., an increase to the lowest $^{13}CH_3D$-based temperature of 158 °C) requires that exchange rates with water be ~1 billion times higher in the Lost City system as compared to the abiotic uncatalyzed rates measured in our study—this was calculated by increasing all rates by a constant multiplicative factor and assuming the same activation energy as from our experiments. For comparison, the measured rate constant in our experiments at 400 °C is calculated to be 1 billion times higher than the rates predicted for 100 °C. Such a rate enhancement would also lead to a measurable decrease in the δD of methane from a starting value of −106‰ (equilibrium at 300 °C with $\delta D_{H2O} = 4‰$) to final value of −122‰. This final value of −122‰ overlaps the range of values measured in the Lost City methane (−99 to −143‰).

Labidi et al. (2020) proposed the change in the isotopic composition of the methane at Lost City may have been catalyzed by microorganisms or on mineral surfaces. Unlike in the higher-temperature fluids examined above (>200 °C exit temperatures), microorganisms are able to exist at the temperatures of the fluids emitted at Lost City and are furthermore known to be present in the carbonate chimney structures (Schrenk et al., 2004; Brazelton et al., 2006). We note that microorganisms have already been argued to enhance the rate of H_2-H_2O isotope exchange at Lost City by orders of magnitude above abiotic rates (Pester et al., 2018). Additionally, as discussed above, methanogens and methanotrophs have both been argued to be able to catalyze hydrogen isotope exchange between CH_4 and H_2O. On this basis, Labidi et al. (2020) proposed microorganisms may play a role in catalyzing methane hydrogen isotope exchange rates at Lost City.

Labidi et al. (2020) also discussed that minerals could act as catalysts for methane hydrogen isotope exchange. They noted γ-Al_2O_3, Ni, and Pt catalysts are known to enhance exchange rates between methane isotopologues or between methane and H_2 (e.g., Larson and Hall, 1965; Stolper et al., 2014b; Ono et al., 2014; Sattler, 2018; Eldridge et al., 2019; Wang et al., 2020; Turner et al., 2021). Such catalysts do enhance C-H exchange, but are commonly poisoned or inactivated in the presence of liquid water (and pure catalytic-grade metals are generally not found in nature). However, such exchange could potentially occur on igneous or secondary minerals in the system. The experiments of Reeves et al. (2012) provide some constraints on this possibility for hydrogen isotope exchange with water. Specifically, their 323 °C experiments included minerals that are common to high-temperature hydrothermal systems: pyrrhotite, pyrite, and magnetite. Compared to the extrapolation of our kinetics to 323 °C, their rate constant (using the best guess estimate rate from Wang et al., 2018) is ~3.9× higher than we would predict, indicating potentially enhanced hydrogen isotope exchange rates due to minerals by a factor of a few, but not 1 billion. However, other minerals (both primary igneous minerals and secondary minerals produced during alteration) in these systems could have different enhancement rates. Regardless, if this explanation is correct, given the catalytic rate enhancement needed, then experiments conducted at temperatures as low as 100–150 °C using minerals found at Lost City and similar water-rock ratios may lead to measurable hydrogen isotope exchange rates comparable to those measured here from 376 to 420 °C.

(ii) Time at peak temperature: The upward movement of deep-seated fluids towards the seafloor in hydrothermal systems requires the fluids to be buoyant. Based on models of fluid flow in mid-ocean ridges, it is thought that fluids become sufficiently buoyant to be vented to the seafloor when they reach temperatures of ~400–425 °C (Jupp and Schultz, 2000; Hasenclever et al., 2014). This concept is sometimes termed 'fluxibility' (Lister, 1995). As such, it is possible that after methane enters or alternatively forms in the fluid of the active hydrothermal system, it may have time to re-equilibrate isotopically before the fluid reaches a temperature and pressure where it is sufficiently buoyant to exit the hydrothermal system and vent to the seafloor. If this occurs, then the isotopic composition of the methane would reflect partially or wholly the temperatures at which the fluid resides at depth and any earlier history of the methane would be overprinted. The residence time of hydrothermal fluids in on-axis systems is commonly estimated to be on the order of years (Kadko and Moore, 1988) as compared to the timescale of hours examined above for upflow and venting of the fluid from depth to the seafloor. These relatively short residence times have also been found in the Lost City system (0.5–2 years; Moore et al., 2021).

To examine this scenario quantitatively, we assume methane enters or is formed in the hydrothermal system with in both clumped isotopic equilibrium and hydrogen isotopic equilibrium with water with a $\delta D_{H2O} = 0‰$ at 300 °C and is then immediately warmed to temperatures between 350 and 500 °C for three years (with water δD kept constant) before emission to the seafloor. The 300 °C used is based on the typical $^{13}CH_3D$-based temperatures of hydrothermal methane from these sorts of systems given in Wang et al. (2018; see discussion above). We use a maximum residence time of three years at each temperature as this timescale is a general estimate for the residence time of high-temperature fluids that reach sufficient temperatures to react with igneous rocks in black-smoker systems (Kadko and Moore, 1988)—this is likely a maximum amount of time at the peak temperature as three years represents the entire residence time for hydrothermal circulation in the system, not just the time at the peak temperature. More specific pathways are not available—they are calculated in models of hydrothermal flow (e.g., Hasenclever et al., 2014) but typical time-temperature pathways are generally not provided.

We provide in Fig. 7 plots of changes in methane δD (Fig. 7A) and $^{13}CH_3D$-based temperatures (Fig. 7B) for these thermal histories. Environmental data is provided for comparison on the right side of each figure. Changes in δD and clumped-isotope temperatures are minimal at temperatures below 375 °C (<1‰ and 11 °C respectively). At temperatures above 375 °C, significant re-equilibration occurs. However, as was the case for the cooling paths discussed above, changes in δD, even when full equilibration is reached (e.g., at 500 °C), are small (<12‰) due to the limited temperature dependence of the equilibrium fractionation factor over this range. In contrast, clumped-isotope temperatures show measurable changes. For example, at temperatures above 425 °C, samples show significant increases in clumped isotope temperature (~65 °C increase at 425 °C after three years). Measured methane clumped-isotope temperatures from these systems are typically ~300 °C (Wang et al., 2018; Labidi et al., 2020) and thus indicate that for the observed systems the vented methane spent insufficient time at temperatures above 400 °C to allow for significant exchange of hydrogen isotopes with water.

(iii) Formation and equilibration of methane outside of the fluid flow: As discussed above, it has been argued that much of the methane vented from marine hydrothermal systems forms outside of the main flow pathways and is subsequently entrained (Welhan and Craig, 1983; Pester et al., 2012; McDermott et al., 2015; Wang et al., 2018;

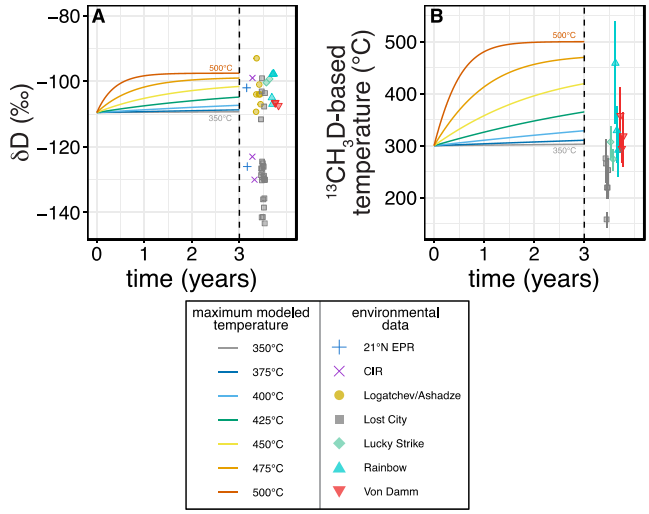

Fig. 7. Calculation of changes in methane (A) δD and (B) $^{13}CH_3D$-based temperature for a system instantaneously heated from an isotopic composition in equilibrium with water ($\delta D_{H2O} = 0‰$) and internal clumped isotopic equilibrium at 300 °C to temperatures from 350 to 500 °C for up to three years. This is done to simulate changes in the isotopic composition of methane during circulation through black-smoker systems. Environmental data (collected while venting to the seafloor) are the same as those in Fig. 6. Error bars are ±1 s.e. or smaller than the size of the data point.

Klein et al., 2019; Grozeva et al., 2020). This exogenous methane is generally proposed to form in fluid inclusions in igneous minerals that later rupture and release methane into the actively circulating hydrothermal system. Methane generation in the inclusions is modeled to occur dominantly at temperatures <340 °C where serpentinization reactions that consume water and produce H_2 are favored. This H_2 can then react with CO_2 to form methane (Klein et al., 2019). As such, the observation that clumped isotope temperatures of hydrothermal methane are typically ~300 °C may be because this is the approximate temperature of peak methane generation in the inclusions. Additionally, calculations based on chemical equilibrium from Klein et al. (2019) predict that 90% of water in the fluid inclusion should be consumed once the system cools below 300 °C (Klein et al., 2019). If the kinetics of the reactions are sufficient for this to occur, the drop in water concentration associated with this loss of water could further slow any isotopic exchange between methane and water below 300 °C and thus act to lock in the commonly observed ~300 °C clumped-isotope based temperatures.

In these inclusions, methane could form in isotopic equilibrium internally and in hydrogen isotopic equilibrium with fluids trapped in the inclusion (e.g., via catalytic exchange reactions during reduction of CO_2 on mineral surfaces), in which case methane δD and the clumped-isotope composition would reflect the dominant temperatures of gas formation along with hydrogen isotopic equilibration with a seawater derived fluid. However, we note that this fluid's isotopic composition could be altered during serpentinization reactions. Alternatively, methane could form out of isotopic equilibrium (i.e., express kinetic isotope effects) and then re-equilibrate isotopically to reflect inclusion temperatures prior to release of CH_4 into the circulating fluid. We can examine the reasonableness of this by calculating the timescale for the methane to reach 99% hydrogen isotopic equilibration with a fluid assuming a fluid density based on the calculations above. For example, the timescale for 99% re-equilibration is ~200 years at 350 °C and ~32,000 years at 250 °C. Given that high-temperature hydrothermal flow is thought to extend out to crust up to ~1 million years old (e.g., Stein and Stein, 1994), we consider it likely that methane in fluid inclusions that contain significant water can reach hydrogen isotopic equilibrium with the water and internal clumped isotopic equilibrium at temperatures of ~300 °C prior to the release of that methane to actively circulating hydrothermal systems.

4.4. High-temperature hydrothermal summary

The above calculations support the previous arguments of Wang et al. (2018) that for high-temperature hydrothermal systems, hydrogen and clumped isotopic compositions of methane are likely established in fluid inclusions initially disconnected from the main hydrothermal flow regime (McDermott et al., 2015; Wang et al., 2018; Klein et al., 2019; Grozeva et al., 2020). Furthermore, the calculated timescales for methane storage in fluid inclusions are likely sufficient for the methane to equilibrate isotopically during storage (and thus reflect storage conditions) before being released into the active flow and vented to the ocean.

5. SUMMARY

We presented the first experimental determinations for the kinetics of hydrogen isotope exchange between methane and supercritical water from 376 to 420 °C. We provided an equation for the temperature dependence of the second-order rate constant that describes this exchange. Our results indicate uncatalyzed exchange with liquid water will not

occur at temperatures below 100–125 °C on geological timescales, but can occur from 125 to 200 °C on order one-million-year timescales, and occurs more rapidly (<100,000 years) at even higher temperatures. Because methanogenic and methanotrophic microorganisms have been proposed to be capable of catalyzing hydrogen isotope exchange reactions between methane and water at low (<122 °C) temperatures, the observation of methane in clumped equilibrium and in hydrogen isotopic equilibrium with water at such low temperatures may be a potential biosignature on Earth (in the present or the past) and on other planetary bodies. We proposed that exchange between thermogenic methane and water at temperatures above 150 °C may allow methane to reach isotopic equilibrium with water and clumped isotopic equilibrium during thermogenic gas formation, which is quenched once gases are expelled and cooled to lower temperatures. Finally, we explored what processes control the isotopic composition of methane from high-temperature hydrothermal systems and found that the derived kinetics are consistent with prior proposals that methane isotopic compositions likely reflect formational conditions outside of the main fluid flow paths and are set during storage in fluid inclusions over thousands to hundreds of thousands of years.

Declaration of Competing Interest

The authors declare that they have no known competing financial interests or personal relationships that could have appeared to influence the work reported in this paper.

ACKNOWLEDGEMENTS

DAS acknowledges support from the National Science Foundation under Grant No. EAR-1911296 and the Donors of the American Chemical Society Petroleum Research Fund. Work at Lawrence Berkeley National Laboratory was supported by the U.S. Department of Energy, Office of Science, Office of Basic Energy Sciences, Chemical Sciences, Geosciences, and Biosciences Division, under Award Number DE-AC02-05CH11231. We thank Shuhei Ono for handling this paper, and Eoghan Reeves, David Wang, and an anonymous reviewer for helpful reviews.

APPENDIX A

A.1 Measurement and standardization of δD_{CH4} values

We measured δD_{CH4} values of experimental samples over the course of ~3.5 years and 13 separate analytical sessions. Individual measurements have the session listed in Table S1. In all sessions, we checked for δD_{CH4} linearity vs. measured peak area. We found that in all cases the slope of δD_{CH4} vs. peak area is not statistically different from zero. Therefore, we did not make linearity corrections for peak area size to data from any analytical session presented in this work.

Over this time, changes were made to our standardization protocol and, as a result, not all sessions were standardized in the same way, which we now discuss. For the first 8 measurement sessions, May 2017 through July 2018, δD_{CH4} were standardized to an in-house methane standard. This methane's δD was determined externally by the UC Davis Stable Isotope Lab following methods in Yarnes (2013) and is anchored to internationally recognized standards. For these sessions, we assumed a constant correction for all samples based on the difference between the measured vs. expected values of the externally calibrated standard. Specifically, we calculated the ratio between the average measured isotopic ratio of our in-house standard and the known isotopic ratio as measured by UC Davis, and used that as a constant multiplicative correction in isotope ratio space before converting samples to δD_{CH4}.

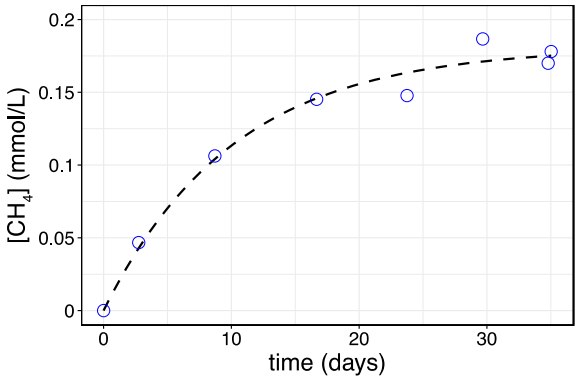

Fig. A1. 400 °C Blank experiment (no methane added, using ~5000‰ water) showing the increase and then leveling off of CH_4 concentration vs. time. Dotted line is a fit to the data of the form $y = a \times [1 - \exp(-x/b)]$ where a and b are constants.

In the November 2018 session, four CH_4 standards were measured (the same described in Turner et al. (2021) and externally measured at UC Davis) with a δD range of −165.7 to +20.0‰. For this session, we corrected samples by linearly regressing raw measured isotopic ratios vs. the known isotopic ratio for each standard. This linear regression was then applied to all sample values in isotope ratio space and then converted back to δD_{CH4}.

In the February 2019 session, two CH_4 standards were measured with similar δD_{CH4} (−165.7‰ and −159.3‰)—both were calibrated externally at UC Davis. Like the May 2017 through July 2018 sessions, for this session we first calculated the ratio between the average measured isotopic ratio of our two in-house standards and the known isotopic ratio as measured by UC Davis and then averaged the two corrections to find the final correction. The correction was applied as described above for the May 2017 through July 2018 sessions.

For the November 2019, July 2020, and October 2020 sessions, combined H_2 and CH_4 standardization was performed following the procedure outlined in Turner et al. (2021).

A.2 Derivation of equations for rates of hydrogen isotope exchange between methane and water

Here we derive the equations that describe the rate of exchange of hydrogen isotopes between methane and water as a function of time. We start with $^{12}CH_3D$ and then move to $^{13}CH_3D$.

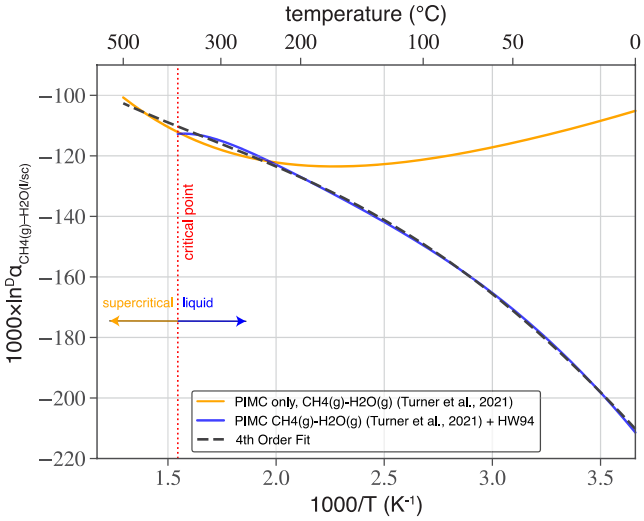

Fig. A2. Black line is the equilibrium 1000 × $\ln^{D}\alpha_{CH4(g)\text{-}H2O(l/sc)}$ vs. 1000/T (K^{-1}) curve used in this study (4th Order Fit, based on theoretical calculations and experimental results determined by Turner et al. (2021) and experimental constraints from Horita and Wesolowski (1994). Arrows drawn indicate which theoretical calculation is used in the 4th order polynomial fit. For temperatures higher than the critical point (374 °C), the DBOC PIMC only calculations from Turner et al. (2021) for gas phase methane and water (shown in orange) are used (offset to fit experimental data). For lower temperatures, the combination of the Turner et al. (2021) DBOC PIMC calculation for CH_4(g)-H_2(g) and H_2(g)-H_2O(g) (both offset to fit experimental data) and Horita and Wesolowski (1994) (HW94) calibration (blue) is used such that the water is in the liquid phase.

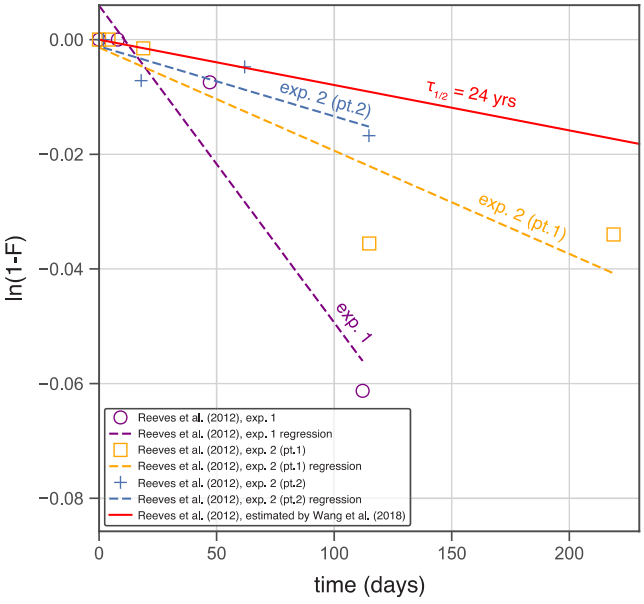

Fig. A3. ln(1 − F) vs. time (days) for methane data presented in Reeves et al. (2012) for the three separate experiments (exp. 1, 2, and 3). ln (1 − F) is calculated using Eq. (3) for $\ln^{D}\alpha_{CH4(g)\text{-}H2O(l/sc)}$ vs. temperature from this manuscript for consistency. Also plotted in red is a calculation based on a 24 year 50% equilibration time ($\tau_{1/2}$), as given in Wang et al. (2018) based on the same data from Reeves et al. (2012) that was used in the regressions.

We begin by examining the following isotope exchange equation:

$$^{12}CH_4 + HDO \underset{k_r}{\overset{k_f}{\rightleftharpoons}} {}^{12}CH_3D + H_2O \tag{A1}$$

This is Eq. (1) in the main text. We assume the overall reaction kinetics are second order and write:

$$\frac{d[\,{}^{12}CH_3D]_t}{dt} = \frac{k_f}{2}[\,{}^{12}CH_4]_t[HDO]_t - \frac{k_r}{4}[\,{}^{12}CH_3D]_t[H_2O]_t \tag{A2}$$

In Eq. (A2), the concentration of the species (in mol/L) is given in brackets at a given time point, t. The rate constants k_r and k_f represent the rate constants for exchange rates of

$^{12}CH_4$ with H_2O to swap an H and are divided by the probability of the exchange actually occurring as written. For example, assuming no kinetic isotope effects, only half of the time that $^{12}CH_4$ and HDO react will a D be transferred such that $^{12}CH_3D$ is created. Similarly, only one quarter of the time will $^{12}CH_3D$ react with H_2O such that a D is transferred from $^{12}CH_3D$ to H_2O and $^{12}CH_4$ formed.

We next assume that for our experiments the concentrations of $^{12}CH_4$, H_2O, and HDO can be treated as constants. For our experimental conditions, the methane:water ratio is at most ~0.003 such that the assumption that the δD of H_2O does not change is valid. We divide both sides by $[^{12}CH_4]$ and manipulate the expression involving [HDO] as follows:

$$\frac{d\left(\frac{^{12}CH_3D}{^{12}CH_4}\right)_t}{dt} = \frac{k_f}{2}[H_2O]\left(\frac{HDO}{H_2O}\right) - \frac{k_r}{4}\left(\frac{^{12}CH_3D}{^{12}CH_4}\right)_t[H_2O] \quad (A3)$$

The subscript t has been dropped from concentrations that are assumed constant. Next, we assume that the relative concentrations of the isotopologues can be approximated by a random distribution of isotopes amongst all isotopologues. This allows us to write:

$$\frac{d\left(\frac{D}{H}\right)_{CH_4,t}}{dt} = \frac{k_f}{4}[H_2O]\left(\frac{D}{H}\right)_{H_2O} - \frac{k_r}{4}\left(\frac{D}{H}\right)_{CH_4,t}[H_2O] \quad (A4)$$

Next, we define the equilibrium hydrogen isotopic distribution between methane and water as:

$$^{D}\alpha_{CH_4-H_2O} = \frac{\left(\frac{D}{H}\right)_{CH_4,eq}}{\left(\frac{D}{H}\right)_{H_2O,eq}} \quad (A5)$$

As the D/H ratio for water is a constant, it is by definition the equilibrium value. Thus (A5) can be substituted into (A4) as follows:

$$\frac{d\left(\frac{D}{H}\right)_{CH_4,\,t}}{dt} = \frac{k_f}{4}[H_2O]\frac{\left(\frac{D}{H}\right)_{CH_4,eq}}{^{D}\alpha_{CH_4-H_2O}} - \frac{k_r}{4}\left(\frac{D}{H}\right)_{CH_4,t}[H_2O] \quad (A6)$$

At isotopic equilibrium, the rate of change of the D/H ratio of methane is 0 and, as such, we can write:

$$k_f = k_r\,^{D}\alpha_{CH_4-H_2O} \quad (A7)$$

We substitute (A7) into (A6) and write:

$$\frac{d\left(\frac{D}{H}\right)_{CH_4,t}}{dt} = \frac{k_r}{4}[H_2O]\left(\frac{D}{H}\right)_{CH_4,eq} - \frac{k_r}{4}\left(\frac{D}{H}\right)_{CH_4,t}[H_2O] \quad (A8)$$

If we integrate and designate the initial concentration of methane with the subscript i we find:

$$\frac{\left(\frac{D}{H}\right)_{CH_4,t} - \left(\frac{D}{H}\right)_{CH_4,eq}}{\left(\frac{D}{H}\right)_{CH_4,i} - \left(\frac{D}{H}\right)_{CH_4,eq}} = e^{-[H_2O]\frac{k_r}{4}t} \quad (A9)$$

This is equivalent to the following equation for the $^{12}CH_3D$ isotopologue:

$$\frac{\left(\frac{^{12}CH_3D}{^{12}CH_4}\right)_t - \left(\frac{^{12}CH_3D}{^{12}CH_4}\right)_{eq}}{\left(\frac{^{12}CH_3D}{^{12}CH_4}\right)_i - \left(\frac{^{12}CH_3D}{^{12}CH_4}\right)_{eq}} = e^{-[H_2O]\frac{k_r}{4}t} \quad (A10)$$

We can then follow convention and incorporate the ¼ term into k_r and manipulate the D/H ratios to be in δ notation and arrive at Eq. (2) of the main text:

$$\frac{\delta D_{CH4}(t) - \delta D_{CH4;\,equilibrium}}{\delta D_{CH4;\,initial} - \delta D_{CH4;\,equilibrium}} = e^{-[H_2O]k_r t} \quad (A11)$$

Next, we show that the rate of exchange for $^{12}CH_3D$ is identical to that for $^{13}CH_3D$ if we assume that there is no difference in isotope effect for hydrogen isotope exchange with a ^{13}C vs ^{12}C bearing species. We write the following isotope exchange reaction:

$$^{13}CH_4 + HDO \underset{k_r}{\overset{k_f}{\rightleftharpoons}} {}^{13}CH_3D + H_2O \quad (A12)$$

We assume that these rate constants are the same as those in (A1). The rate of change of $^{13}CH_3D$ vs. time can be written as.

$$\frac{d[\,^{13}CH_3D]_t}{dt} = \frac{k_f}{2}[\,^{13}CH_4]_t[HDO]_t - \frac{k_r}{4}[\,^{13}CH_3D]_t[H_2O]_t \quad (A13)$$

We assume that the $^{13}CH_4$ concentration is constant and the hydrogen isotopic composition of the water is also constant (as discussed above). We additionally assume that the unsubstituted and singly substituted isotopologues of methane and water at equilibrium can be approximated as being at a random isotopic distribution (as above). This allows us to rewrite Eq. (A13) as:

$$\frac{d\left(\frac{^{13}CH_3D}{^{12}CH_4}\right)_t}{dt} = \frac{k_f}{4\,^{D}\alpha_{CH_4-H_2O}}[H_2O]\left(\frac{^{13}CH_4}{^{12}CH_4}\right)_{eq}\left(\frac{^{12}CH_3D}{^{12}CH_4}\right)_{eq} - \frac{k_r}{4}\left(\frac{^{13}CH_3D}{^{12}CH_4}\right)_t[H_2O] \quad (A14)$$

When isotopic equilibrium is reached, k_f and k_r are related as follows:

$$k_f = k_r\,^{D}\alpha_{CH_4-H_2O}\frac{\left(\frac{^{13}CH_3D}{^{12}CH_4}\right)_{eq}}{\left(\frac{^{13}CH_3D}{^{12}CH_4}\right)_{eq}\left(\frac{^{12}CH_3D}{^{12}CH_4}\right)_{eq}} \quad (A15)$$

When (A15) is substituted into (A14), we find:

$$\frac{d\left(\frac{^{13}CH_3D}{^{12}CH_4}\right)_t}{dt} = \frac{k_r}{4}[H_2O]\left(\frac{^{13}CH_3D}{^{12}CH_4}\right)_{eq} - \frac{k_r}{4}\left(\frac{^{13}CH_3D}{^{12}CH_4}\right)_t[H_2O] \quad (A16)$$

Integration of this yields:

$$\frac{\left(\frac{^{13}CH_3D}{^{12}CH_4}\right)_t - \left(\frac{^{13}CH_3D}{^{12}CH_4}\right)_{eq}}{\left(\frac{^{13}CH_3D}{^{12}CH_4}\right)_i - \left(\frac{^{13}CH_3D}{^{12}CH_4}\right)_{eq}} = e^{-[H_2O]\frac{k_r}{4}t} \quad (A17)$$

The right side of Eq. (A17) is identical to that for the evolution of $^{12}CH_3D$ (Eq. (A10)) showing they equilibrate (fractionally) at the same rates given the assumptions above.

When modeling $^{13}CH_3D$ clumped isotopic compositions, we calculate both the equilibrium isotopic composition and convert modeled $^{13}CH_3D$ concentrations to apparent temperatures based the equations given in Eldridge et al. (2019).

For the calculations conducted in the main text in which a thermal history is calculated, we forward integrate Eqs. (A8) and (A16) using the MATLAB ode15s solver.

A.3 Calculation of the equilibrium fractionation factor between methane and liquid/supercritical water as a function of temperature

Use of Eqs. (2) and (4) to derive rate constants requires knowledge of the equilibrium $^{D}\alpha_{CH4(g)\text{-}H2O(l/sc)}$ at a given temperature. Over the temperature range of this study, there is one set of experimental constraints on $^{D}\alpha_{CH4(g)\text{-}H2O(l)}$, which is given by Horibe and Craig (1995). This was calculated using $^{D}\alpha_{CH4(g)\text{-}H2(g)}$ experimentally determined by them (Horibe and Craig, 1995) combined with $^{D}\alpha_{H2O(g)\text{-}H2(g)}$ as determined by Suess (1949) and $^{D}\alpha_{H2O(l)\text{-}H2O(g)}$ from Horita and Wesolowski (1994). In this study, however, we do not use this for two reasons. First, the equation given in Horita and Wesolowski (1994) can only interpolated from 0 to 374 °C and the form of the equation is not suitable for extrapolation to the higher temperatures of our experiments as well as modeled systems. Additionally, we have shown that this calibration deviates from work done in our laboratory by 22.9‰ at 200 °C indicating potential interlaboratory offsets. This latter point is discussed in Turner et al. (2021).

Instead, we use the Path-Integral Monte Carlo (PIMC) theoretical calculations from Turner et al. (2021) that are offset to fit our prior experimental constraints. Such an approach is based on that given in Clayton and Kieffer (1991) where theoretical calculations of equilibrium isotopic fractionation factors are offset to fit experimental data in order to allow for extrapolations beyond experimentally calibrated temperature using theoretically expected temperature dependencies.

Here we first took the 4th order polynomial fit to theoretical (diagonal Born-Oppenheimer corrected [DBOC] PIMC) calculations for $1000 \times \ln^{D}\alpha_{CH4(g)\text{-}H2(g)}$ vs. 1/T as given in Turner et al. (2021) (Table EA6) and applied a constant offset of +1.9‰. This offset was determined by a least squares fit of the theoretical calibration to the CH_4-H_2 experimental data given in Turner et al. (2021). These experimental determinations span a temperature range of 3–200 °C. The least squares fitting follows that described in Sections 3.4, 3.6, and Appendix 2 of Turner et al. (2021). This equation was then combined with the DBOC PIMC calculations of $1000 \times \ln^{D}\alpha_{H2O(g)\text{-}H2(g)}$ given in Turner et al. (2021; Table EA6). As described in that paper, these were also linearly offset to fit experimental H_2O-H_2 data (by +0.49‰; see Section 3.4 of that work).

Together these provide a polynomial expression for the temperature dependence of $1000 \times \ln^{D}\alpha_{CH4(g)\text{-}H2O(g)}$. We convert $1000 \times \ln^{D}\alpha_{CH4(g)\text{-}H2O(g)}$ to $1000 \times \ln^{D}\alpha_{CH4(g)\text{-}H2O(l/sc)}$ by adding the polynomial expression for $1000 \times \ln^{D}\alpha_{H2O(l)\text{-}H2O(g)}$ given in Horita and Wesolowski (1994) for temperatures below the critical point of pure water (374 °C). At temperatures above the critical point, we assume no isotopic difference between a supercritical fluid and an ideal gas and thus use our calibration for $1000 \times \ln^{D}\alpha_{CH4(g)\text{-}H2O(g)}$ for supercritical phases—inaccuracies associated with this assumption are discussed in the main text. These combined $1000 \times \ln^{D}\alpha_{CH4(g)\text{-}H2O(l/sc)}$ estimates were calculated from 0 to 500 °C at a temperature step of 0.1 °C and the values were then regressed using a 4th order polynomial regression vs. 1/T (K) (Fig. A2). We note that an apparent kink occurs as one transitions from the water to supercritical regime (374 °C), which we associate with our assumption that supercritical fluids can be approximated as ideal gases for hydrogen isotope fractionations with methane gas. Maximum difference between the polynomial fit and calculated values is 2.48‰, which we consider to be negligible for the calculations presented here.

A.4 Treatment of data from experiments with leaks

Experiment 4 part 1 and part 2 and experiment 6 were observed to have leaks between the inside of the gold cell and the outside confining water (changes in δD_{H2O} of ~192‰, ~398‰, and ~1290‰ respectively based on taking the difference between the value at maximum and minimum time from linear regression of δD_{H2O} vs. time for each experiment). Leaks were observed and quantified through measurement of the δD_{H2O} of the internal gold cell fluid from samples taken over the course of the experiments (these experiments did not include krypton as a secondary check—krypton was added in later experiments, which did not measurably leak). For the fits, we used the time-weighted average of the measured δD_{H2O} to calculate the equilibrium δD_{CH4} value for use in Eq. (4).

We verified this approach was acceptable as follows: We created a forward model to test the effect of calculating $\ln(k_r)$ in a system in which the δD_{H2O} changes with time (e.g., due to a leak). We prescribe the 'true' $\ln(k_r)$ value, the initial δD_{H2O}, the rate of change of δD_{H2O} over time, and the initial δD_{CH4}. We used these to forward model via numerical integration the progression of δD_{CH4} with time and take into account the change in δD_{H2O}. We then took the time-weighted average of all measured δD_{H2O} values and treated this value as a constant δD_{H2O} in our calculation of $^{D}\alpha_{CH4(g)\text{-}H2O(l/sc)}$ and calculated the rate constant based on the change in δD_{CH4} using Eq. (4). We found the difference between the true value for k_r vs. that we calculated to be sufficiently small as to not matter for the determined values of k_r as we now explain.

As an example, we used parameters and $\ln(k_r)$ values based on the measured values in Experiment 6, which has the largest change in δD_{H2O} due to a leak. In this calculation, we used parameters analogous to the portion of the

experiment used to calculate our $\ln(k_r)$ (i.e., from 10 days until the end of the experiment at 125 days). The input parameters for the calculation are as follows: 'true' $\ln(k_r) = -21.92$, initial $\delta D_{CH4} = -143‰$, initial $\delta D_{H2O} = 4270‰$ (based on a linear regression of the experimental δD_{H2O} vs. time from 10 to 125 days), total change in δD_{H2O} over the 115 used days of the experiment of 1290‰ (final δD_{H2O} of 2980‰). Calculations were forward integrated at 0.1 hr timesteps and the time weighted average water δD_{H2O} calculated and then used in the calculation of $\ln(k_r)$. We find the calculated $\ln(k_r)$ is 0.0018 log units more negative than the true value, which is less than the ±2 s.e. uncertainty of our determination of this value using the experimental data (±0.016). We conducted this for every experiment with a leak and verified that the inaccuracy of using the average δD_{H2O} is less than the ±2 s.e. uncertainty of the determined value of k_r from the experimental data.

A.5 Monte Carlo error propagation scheme

We quantified the uncertainty for our calculated rate constants using a Monte Carlo error propagation scheme. This was done to take into account uncertainty in measured δD values of methane and water. For a given experiment, we take the measured time, δD_{CH4}, and δD_{H2O} and create one million different datasets. In each dataset, for a given data point, we calculate the δD value for that Monte Carlo simulation based on the measured δD combined with ±1σ measurement uncertainty sampled from a Gaussian distribution. This simulated uncertainty is ±2‰ (1σ) for methane (based on the 1σ for measured standards) and at minimum ±15‰ (1σ) for water. This minimum for water δD is estimated using a separate Monte Carlo error propagation to combine uncertainty resulting from the combination of measurement precision and the 10× dilution required to make the measurements. The measured ±1σ for our δD_{H2O} determinations (in those experiments which did not leak) varies between 5.9‰ and 49.7‰. If the measured ±1σ is less than 15‰, we substitute 15‰ in the Monte Carlo calculations as the ±1σ uncertainty. If the measured uncertainty is larger than ±15‰ (1σ), we use that larger value in the Monte Carlo simulations. For experiments that leaked, we use the maximum measured $\delta D_{H2O} \pm 1\sigma$ (49.7‰) as the estimate. We then regress all data sets using Eq. (4) and calculate the mean and ±1σ of the value for $\ln(k_r)$. From this we calculate k_r and the associated uncertainty as given in Table 1. We compared this estimate to the ±1 s.e. from the linear regression and in all cases this Monte Carle estimate is larger. We therefore use the larger Monte Carle estimate of the uncertainty.

APPENDIX B. SUPPLEMENTARY MATERIAL

Supplementary data to this article can be found online at https://doi.org/10.1016/j.gca.2022.04.029.

REFERENCES

Beaudry P., Stefánsson A., Fiebig J., Rhim J. H. and Ono S. (2021) High temperature generation and equilibration of methane in terrestrial geothermal systems: Evidence from clumped isotopologues. *Geochim. Cosmochim. Acta* **309**, 209–234.

Brazelton W. J., Schrenk M. O., Kelley D. S. and Baross J. A. (2006) Methane-and sulfur-metabolizing microbial communities dominate the Lost City hydrothermal field ecosystem. *Appl. Environ. Microbiol.* **72**, 6257–6270.

Burruss R. and Laughrey C. (2010) Carbon and hydrogen isotopic reversals in deep basin gas: Evidence for limits to the stability of hydrocarbons. *Org. Geochem.* **41**, 1285–1296.

Clayton R. N. and Kieffer S. W. (1991) Oxygen isotopic thermometer calibrations. In *Stable Isotope Geochemistry: A Tribute to Samuel Epstein*, pp. 3–10.

Criss R. E. (1999) *Principles of Stable Isotope Distribution*. Oxford University Press, New York.

Criss R., Gregory R. and Taylor, Jr., H. (1987) Kinetic theory of oxygen isotopic exchange between minerals and water. *Geochim. Cosmochim. Acta* **51**, 1099–1108.

Dong G., Xie H., Formolo M., Lawson M., Sessions A. and Eiler J. (2021) Clumped isotope effects of thermogenic methane formation: Insights from pyrolysis of hydrocarbons. *Geochim. Cosmochim. Acta* **303**, 159–183.

Douglas P. M., Stolper D. A., Eiler J. M., Sessions A. L., Lawson M., Shuai Y., Bishop A., Podlaha O. G., Ferreira A. A. and Neto E. V. S. (2017) Methane clumped isotopes: Progress and potential for a new isotopic tracer. *Org. Geochem.* **113**, 262–282.

Douglas P., Stolper D., Smith D., Anthony K. W., Paull C., Dallimore S., Wik M., Crill P., Winterdahl M. and Eiler J. (2016) Diverse origins of Arctic and Subarctic methane point source emissions identified with multiply-substituted isotopologues. *Geochim. Cosmochim. Acta* **188**, 163–188.

Driesner T. (2007) The system H_2O–NaCl. Part II: Correlations for molar volume, enthalpy, and isobaric heat capacity from 0 to 1000 C, 1 to 5000 bar, and 0 to 1 XNaCl. *Geochim. Cosmochim. Acta* **71**, 4902–4919.

Driesner T. and Heinrich C. A. (2007) The system H_2O–NaCl. Part I: Correlation formulae for phase relations in temperature–pressure–composition space from 0 to 1000 C, 0 to 5000 bar, and 0 to 1 XNaCl. *Geochim. Cosmochim. Acta* **71**, 4880–4901.

Duan Z. and Mao S. (2006) A thermodynamic model for calculating methane solubility, density and gas phase composition of methane-bearing aqueous fluids from 273 to 523 K and from 1 to 2000 bar. *Geochim. Cosmochim. Acta* **70**, 3369–3386.

Eiler J. M. (2007) "Clumped-isotope" geochemistry - The study of naturally-occurring, multiply-substituted isotopologues. *Earth Planet. Sci. Lett.* **262**, 309–327.

Eldridge D. L., Korol R., Lloyd M. K., Turner A. C., Webb M. A., Miller, III, T. F. and Stolper D. A. (2019) Comparison of experimental vs theoretical abundances of $^{13}CH_3D$ and $^{12}CH_2D_2$ for isotopically equilibrated systems from 1 to 500 °C. *ACS Earth Space Chem.* **3**, 2747–2764.

Foustoukos D. I. and Seyfried W. E. (2007) Quartz solubility in the two-phase and critical region of the NaCl–KCl–H_2O system: Implications for submarine hydrothermal vent systems at 9 50′ N East Pacific Rise. *Geochim. Cosmochim. Acta* **71**, 186–201.

Giunta T., Labidi J., Kohl I. E., Ruffine L., Donval J. P., Géli L., Çağatay M. N., Lu H. and Young E. D. (2021) Evidence for methane isotopic bond re-ordering in gas reservoirs sourcing cold seeps from the Sea of Marmara. *Earth Planet. Sci. Lett.* **553,** 116619.

Giunta T., Young E. D., Warr O., Kohl I., Ash J. L., Martini A., Mundle S. O., Rumble D., Pérez-Rodríguez I. and Wasley M. (2019) Methane sources and sinks in continental sedimentary systems: New insights from paired clumped isotopologues $^{13}CH_3D$ and $^{12}CH_2D_2$. *Geochim. Cosmochim. Acta* **245**, 327–351.

Gregory R. T., Criss R. E. and Taylor, Jr., H. P. (1989) Oxygen isotope exchange kinetics of mineral pairs in closed and open systems: Applications to problems of hydrothermal alteration of igneous rocks and Precambrian iron formations. *Chem. Geol.* **75**, 1–42.

Gropp J., Iron M. A. and Halevy I. (2021) Theoretical estimates of equilibrium carbon and hydrogen isotope effects in microbial methane production and anaerobic oxidation of methane. *Geochim. Cosmochim. Acta* **295**, 237–264.

Grozeva N. G., Klein F., Seewald J. S. and Sylva S. P. (2020) Chemical and isotopic analyses of hydrocarbon-bearing fluid inclusions in olivine-rich rocks. *Philos. Trans. R. Soc. A* **378,** (2165).

Hasenclever J., Theissen-Krah S., Rüpke L. H., Morgan J. P., Iyer K., Petersen S. and Devey C. W. (2014) Hybrid shallow on-axis and deep off-axis hydrothermal circulation at fast-spreading ridges. *Nature* **508**, 508–512.

Hoering T. (1984) Thermal reactions of kerogen with added water, heavy water and pure organic substances. *Org. Geochem.* **5**, 267–278.

Horibe Y. and Craig H. (1995) D/H fractionation in the system methane-hydrogen-water. *Geochim. Cosmochim. Acta* **59**, 5209–5217.

Horita J. and Wesolowski D. J. (1994) Liquid-vapor fractionation of oxygen and hydrogen isotopes of water from the freezing to the critical temperature. *Geochim. Cosmochim. Acta* **58**, 3425–3437.

Hunt J. M. (1996) *Petroleum Geochemistry and Geology*. W. H. Freeman and Company, New York.

Ijiri A., Inagaki F., Kubo Y., Adhikari R. R., Hattori S., Hoshino T., Imachi H., Kawagucci S., Morono Y., Ohtomo Y., Ono S., Sakai S., Takai K., Toki T., Wang D. T., Yoshinaga M. Y., Arnold G. L., Ashi J., Case D. H., Feseker T., Hinrichs K.-U., Ikegawa Y., Ikehara M., Kallmeyer J., Kumagai H., Lever M. A., Morita S., Nakamura K., Nakamura Y., Nishizawa M., Orphan V. J., Røy H., Schmidt F., Tani A., Tanikawa W., Terada T., Tomaru H., Tsuji T., Tsunogai U., Yamaguchi Y. T. and Yoshida N. (2018) Deep-biosphere methane production stimulated by geofluids in the Nankai accretionary complex. *Sci. Adv.* **4**, eaao4631.

Jautzy J. J., Douglas P. M., Xie H., Eiler J. M. and Clark I. D. (2021) CH4 isotopic ordering records ultra-slow hydrocarbon biodegradation in the deep subsurface. *Earth Planet. Sci. Lett.* **562,** 116841.

Jupp T. and Schultz A. (2000) A thermodynamic explanation for black smoker temperatures. *Nature* **403**, 880–883.

Kadko D. and Moore W. (1988) Radiochemical constraints on the crustal residence time of submarine hydrothermal fluids: Endeavour Ridge. *Geochim. Cosmochim. Acta* **52**, 659–668.

Kawagucci S., Miyazaki J., Noguchi T., Okamura K., Shibuya T., Watsuji T., Nishizawa M., Watanabe H., Okino K. and Takahata N. (2016) Fluid chemistry in the Solitaire and Dodo hydrothermal fields of the Central Indian Ridge. *Geofluids* **16**, 988–1005.

Klein F., Grozeva N. G. and Seewald J. S. (2019) Abiotic methane synthesis and serpentinization in olivine-hosted fluid inclusions. *Proc. Natl. Acad. Sci.* **116**, 17666–17672.

Koepp M. (1978) D/H isotope exchange reaction between petroleum and water: A contributory determinant for D/H-isotope ratios in crude oils. In *In The Fourth International Conference, Geochronology, Cosmochronology, Isotope Geology USGS Open-File Report 78*, pp. 221–222.

Konn C., Charlou J. L., Holm N. G. and Mousis O. (2015) The production of methane, hydrogen, and organic compounds in ultramafic-hosted hydrothermal vents of the Mid-Atlantic Ridge. *Astrobiology* **15**, 381–399.

Köpp M. (1977) D/H-Isotopenaustausch Zwischen Kohlenwasserstoffen und Deuteriumoxid - Schaffung Der Experimentellen Voraussetzungen Und Erste Ergebnisse, Berichet D 1.1. In *D/H-Isotopenverhältnisse in organischen Substanzen, Erdölen und Erdgasen, Bericht I* Forschungsvorhaben ET 3003A, Hannover.

Köpp M. (1978) Experimentelle Bestimmung Der D/H-Isotopenaustauschraten Zwischen Kohlenwasserstoffen Und Wasser, Berichet D 1.2. In *D/H-Isotopenverhältnisse in organischen Substanzen, Erdölen und Erdgasen, Bericht I* Forschungsvorhaben ET 3003A, Hannover.

Labidi J., Young E. D., Giunta T., Kohl I. E., Seewald J., Tang H., Lilley M. D. and Früh-Green G. L. (2020) Methane thermometry in deep-sea hydrothermal systems: Evidence for re-ordering of doubly-substituted isotopologues during fluid cooling. *Geochim. Cosmochim. Acta* **288**, 248–261.

Larson J. G. and Hall W. K. (1965) Studies of the hydrogen held by solids. VII. The exchange of the hydroxyl groups of alumina and silica-alumina catalysts with deuterated methane. *J. Phys. Chem.* **69**, 3080–3089.

Lazar C., Cody G. D. and Davis J. M. (2015) A kinetic pressure effect on the experimental abiotic reduction of aqueous CO_2 to methane from 1 to 3.5 kbar at 300 °C. *Geochim. Cosmochim. Acta* **151**, 34–48.

Lewan M. (1997) Experiments on the role of water in petroleum formation. *Geochim. Cosmochim. Acta* **61**, 3691–3723.

Lister C. R. B. (1995) Heat transfer between magmatism and hydrothermal systems, or, six lemmas in search of a theorem. *Geophys. J. Int.* **120**, 45–59.

Lollar B. S., Lacrampe-Couloume G., Voglesonger K., Onstott T. C., Pratt L. M. and Slater G. F. (2008) Isotopic signatures of CH4 and higher hydrocarbon gases from Precambrian Shield sites: A model for abiogenic polymerization of hydrocarbons. *Geochim. Cosmochim. Acta* **72**, 4778–4795.

Mangenot X., Tarantola A., Mullis J., Girard J.-P., Le V.-H. and Eiler J. M. (2021) Geochemistry of clumped isotopologues of CH4 within fluid inclusions in Alpine tectonic quartz fissures. *Earth Planet. Sci. Lett.* **561,** 116792.

McCollom T. (2012) Methane generation during experimental serpentinization of olivine. *Proc. Natl. Acad. Sci.* **109**, E3334.

McDermott J. M., Seewald J. S., German C. R. and Sylva S. P. (2015) Pathways for abiotic organic synthesis at submarine hydrothermal fields. *Proc. Natl. Acad. Sci.* **112**, 7668–7672.

McDermott J. M., Sylva S. P., Ono S., German C. R. and Seewald J. S. (2018) Geochemistry of fluids from Earth's deepest ridge-crest hot-springs: Piccard hydrothermal field, Mid-Cayman Rise. *Geochim. Cosmochim. Acta* **228**, 95–118.

Moore W. S., Frankle J. D., Benitez-Nelson C. R., Früh-Green G. L. and Lang S. Q. (2021) Activities of ^{223}Ra and ^{226}Ra in fluids from the lost city hydrothermal field require short fluid residence times. *J. Geophys. Res. Oceans* **126**, e2021JC017886.

Okumura T., Kawagucci S., Saito Y., Matsui Y., Takai K. and Imachi H. (2016) Hydrogen and carbon isotope systematics in hydrogenotrophic methanogenesis under H_2-limited and H_2-enriched conditions: Implications for the origin of methane and its isotopic diagnosis. *Prog. Earth Planet. Sci.* 3, doi: 10.1186/s40645-016-0088-3.

Ono S., Rhim J. H., Gruen D. S., Taubner H., Kölling M. and Wegener G. (2021) Clumped isotopologue fractionation by microbial cultures performing the anaerobic oxidation of methane. *Geochim. Cosmochim. Acta* **293**, 70–85.

Ono S., Wang D. T., Gruen D. S., Sherwood L. B., Zahniser M. S., McManus B. J. and Nelson D. D. (2014) Measurement of a doubly substituted methane isotopologue, $^{13}CH_3D$, by tunable infrared laser direct absorption spectroscopy. *Anal. Chem.* **86**, 6487–6494.

Pepper A. S. and Corvi P. J. (1995) Simple kinetic models of petroleum formation. Part III: Modelling an open system. *Mar. Pet. Geol.* **12**, 417–452.

Pester N. J., Conrad M. E., Knauss K. G. and DePaolo D. J. (2018) Kinetics of D/H isotope fractionation between molecular hydrogen and water. *Geochim. Cosmochim. Acta* **242**, 191–212.

Pester N. J., Reeves E. P., Rough M. E., Ding K., Seewald J. S. and Seyfried, Jr., W. E. (2012) Subseafloor phase equilibria in high-temperature hydrothermal fluids of the Lucky Strike Seamount (Mid-Atlantic Ridge, 37 17′ N). *Geochim. Cosmochim. Acta* **90**, 303–322.

Pester N. J., Rough M., Ding K. and Seyfried, Jr., W. E. (2011) A new Fe/Mn geothermometer for hydrothermal systems: Implications for high-salinity fluids at 13 N on the East Pacific Rise. *Geochim. Cosmochim. Acta* **75**, 7881–7892.

Polyakov V. B., Horita J. and Cole D. R. (2006) Pressure effects on the reduced partition function ratio for hydrogen isotopes in water. *Geochim. Cosmochim. Acta* **70**, 1904–1913.

Proskurowski G., Lilley M. D., Kelley D. S. and Olson E. J. (2006) Low temperature volatile production at the Lost City Hydrothermal Field, evidence from a hydrogen stable isotope geothermometer. *Chem. Geol.* **229**, 331–343.

Quigley T. and Mackenzie A. (1988) The temperatures of oil and gas formation in the sub-surface. *Nature* **333**, 549–552.

Reeves E. P., Seewald J. S. and Sylva S. P. (2012) Hydrogen isotope exchange between n-alkanes and water under hydrothermal conditions. *Geochim. Cosmochim. Acta* **77**, 582–599.

Sandvik E. I., Young W. A. and Curry D. J. (1992) Expulsion from hydrocarbon sources: The role of organic absorption. *Org. Geochem.* **19**, 77–87.

Sattler A. (2018) Hydrogen/Deuterium (H/D) exchange catalysis in alkanes. *ACS Catal.* **8**, 2296–2312.

Scheuermann P. P., Tan C. and Seyfried, Jr., W. E. (2018) Quartz solubility in the two-phase region of the NaCl-H_2O system: An experimental study with application to the Piccard hydrothermal field, mid-cayman rise. *Geochem. Geophys. Geosyst.* **19**, 3570–3582.

Schimmelmann A., Sessions A. L. and Mastalerz M. (2006) Hydrogen isotopic (D/H) composition of organic matter during diagenesis and thermal maturation. *Annu. Rev. Earth Planet Sci.* **34**, 501–533.

Schrenk M. O., Kelley D. S., Bolton S. A. and Baross J. A. (2004) Low archaeal diversity linked to subseafloor geochemical processes at the Lost City Hydrothermal Field, Mid-Atlantic Ridge. *Environ. Microbiol.* **6**, 1086–1095.

Seewald J. S. (2003) Organic–inorganic interactions in petroleum-producing sedimentary basins. *Nature* **426**, 327–333.

Seewald J. S., Benitez-Nelson B. C. and Whelan J. K. (1998) Laboratory and theoretical constraints on the generation and composition of natural gas. *Geochim. Cosmochim. Acta* **62**, 1599–1617.

Seyfried W. E., Pester N. J., Tutolo B. M. and Ding K. (2015) The Lost City hydrothermal system: Constraints imposed by vent fluid chemistry and reaction path models on subseafloor heat and mass transfer processes. *Geochim. Cosmochim. Acta* **163**, 59–79.

Seyfried W., Gordon P. and Dickson F. (1979) A new reaction cell for hydrothermal solution equipment. *Am. Mineral.* **64**, 646–649.

Shuai Y., Douglas P. M. J., Zhang S., Stolper D. A., Ellis G. S., Lawson M., Lewan M., Formolo M., Mi J., He K., Hu G. and Eiler J. M. (2018) Equilibrium and non-equilibrium controls on the abundances of clumped isotopologues of methane during thermogenic formation in laboratory experiments: Implications for the chemistry of pyrolysis and the origins of natural gases. *Geochim. Cosmochim. Acta* **223**, 159–174.

Stein C. A. and Stein S. (1994) Constraints on hydrothermal heat flux through the oceanic lithosphere from global heat flow. *J. Geophys. Res. Solid Earth* **99**, 3081–3095.

Stolper D. A., Lawson M., Davis C., Ferreira A., Neto E. S., Ellis G., Lewan M., Martini A., Tang Y. and Schoell M. (2014a) Formation temperatures of thermogenic and biogenic methane. *Science* **344**, 1500–1503.

Stolper D. A., Sessions A. L., Ferreira A., Santos Neto E. V., Schimmelmann A., Shusta S. S., Valentine D. L. and Eiler J. M. (2014b) Combined ^{13}C-D and D-D clumping in methane: Methods and preliminary results. *Geochim. Cosmochim. Acta* **126**, 169–191.

Stolper D., Lawson M., Davis C., Douglas P. and Eiler J. (2018) The utility of methane clumped isotopes to constrain the origins of methane in natural-gas accumulations. *Geol. Soc. Lond.* **468**, 23–52.

Stolper D., Martini A., Clog M., Douglas P., Shusta S., Valentine D., Sessions A. and Eiler J. (2015) Distinguishing and understanding thermogenic and biogenic sources of methane using multiply substituted isotopologues. *Geochim. Cosmochim. Acta* **161**, 219–247.

Suess H. E. (1949) Das Gleichgewicht $H_2 + HDO \rightleftharpoons HD + H_2O$ und die weiteren Austauschgleichgewichte im System H_2, D_2 und H_2O. *Z. Für Naturforschung A* **4**, 328–332.

Takai K., Nakamura K., Toki T., Tsunogai U., Miyazaki M., Miyazaki J., Hirayama H., Nakagawa S., Nunoura T. and Horikoshi K. (2008) Cell proliferation at 122 °C and isotopically heavy CH_4 production by a hyperthermophilic methanogen under high-pressure cultivation. *Proc. Natl. Acad. Sci.* **105**, 10949–10954.

Turner A. C., Korol R., Eldridge D. L., Bill M., Conrad M., Miller, III, T. F. and Stolper D. A. (2021) Experimental and theoretical determinations of hydrogen isotopic equilibrium in the system CH_4-H_2-H_2O from 3 to 200 °C. *Geochim. Cosmochim. Acta* **314**, 223–269.

Von Damm K. L., Lilley M. D., Shanks, III, W. C., Brockington M., Bray A. M., O'grady K. M., Olson E., Graham A. and Proskurowski G. (2003) Extraordinary phase separation and segregation in vent fluids from the southern East Pacific Rise. *Earth Planet. Sci. Lett.* **206**, 365–378.

Wang D. T., Gruen D. S., Sherwood L. B., Hinrichs K.-U., Stewart L. C., Holden J. F., Hristov A. N., Pohlman J. W., Morrill P. L., Konneke M., Delwiche K. B., Reeves E. P., Sutcliffe C. N., Ritter D. J., Seewald J. S., McIntosh J. C., Hemond H. F., Kubo M. D., Cardace D., Hoehler T. M. and Ono S. (2015) Nonequilibrium clumped isotope signals in microbial methane. *Science* **348**, 428–431.

Wang D. T., Reeves E. P., McDermott J. M., Seewald J. S. and Ono S. (2018) Clumped isotopologue constraints on the origin of methane at seafloor hot springs. *Geochim. Cosmochim. Acta* **223**, 141–158.

Wang D. T., Sattler A., Paccagnini M. and Chen F. G. (2020) Method for calibrating methane clumped isotope measurements via catalytic equilibration of methane isotopologues on γ-alumina. *Rapid Commun. Mass Spectrom.* **34**(10), e8555.

Warr O., Sherwood L. B., Fellowes J., Sutcliffe C. N., McDermott J. M., Holland G., Mabry J. C. and Ballentine C. J. (2018) Tracing ancient hydrogeological fracture network age and compartmentalisation using noble gases. *Geochim. Cosmochim. Acta* **222**, 340–362.

Watt W. S., Borrell P., Lewis D. and Bauer S. H. (1966) Isotope exchange rates. IV. The homogeneous reaction between CH_4 and D_2. *J. Chem. Phys.* **45**, 444–450.

Wegener G., Gropp J., Taubner H., Halevy I. and Elvert M. (2021) Sulfate-dependent reversibility of intracellular reactions

explains the opposing isotope effects in the anaerobic oxidation of methane. *Sci. Adv.* **7,** eabe4939..

Welhan J. A. and Craig H. (1983) Methane, hydrogen and helium in hydrothermal fluids at 21°N on the East Pacific Rise. In *Hydrothermal Processes at Seafloor Spreading Centers* (eds. P. A. Rona, K. Boström, L. Laubier and K. L. Smith), NATO Conference Series. Springer US, Boston, MA, pp. 391–409.

Wilcock W. S. (2004) Physical response of mid-ocean ridge hydrothermal systems to local earthquakes. *Geochem. Geophys. Geosyst.* 5, doi: 10.1029/2004GC000701.

Xie H., Dong G., Formolo M., Lawson M., Liu J., Cong F., Mangenot X., Shuai Y., Ponton C. and Eiler J. (2021) The evolution of intra-and inter-molecular isotope equilibria in natural gases with thermal maturation. *Geochim. Cosmochim. Acta* **307**, 22–41.

Yarnes C. (2013) $\delta^{13}C$ and $\delta^{2}H$ measurement of methane from ecological and geological sources by gas chromatography/combustion/pyrolysis isotope-ratio mass spectrometry. *Rapid Commun. Mass Spectrom.* **27**, 1036–1044.

Young E., Kohl I., Lollar B. S., Etiope G., Rumble D., Li S., Haghnegahdar M., Schauble E., McCain K. and Foustoukos D. (2017) The relative abundances of resolved $^{12}CH_2D_2$ and $^{13}CH_3D$ and mechanisms controlling isotopic bond ordering in abiotic and biotic methane gases. *Geochim. Cosmochim. Acta* **203**, 235–264.

Zhang Y. (2008) *Geochemical Kinetics*. Princeton University Press.

Zhong D., Franke J.-H., Podiyanachari S. K., Blömker T., Zhang H., Kehr G., Erker G., Fuchs H. and Chi L. (2011) Linear alkane polymerization on a gold surface. *Science* **334**, 213–216.

Associate editor: Shuhei Ono